3D micro-mechanics of a CFRP laminate under high-rate and varying temperature loading using digital volume correlation

ARTICLE INFO

Keywords:
Fibre-reinforced-polymer composites
Impact behaviour
Temperature effects
Synchrotron X-ray tomography
Digital volume correlation (DVC)
Microscopic strain analysis
Damage micro-mechanics

ABSTRACT

Understanding microscopic damage mechanics in laminated CFRP at high-strain-rate (HSR) loading and extreme temperatures remains an enduring challenge. Using X-ray tomography coupled with digital volume correlation (DVC), three-dimensional local displacement/strain fields and segmented micron-scale intra-ply cracking were quantified, revealing damage micro-mechanics at HSR. Local deformation exhibits strong directionality that intensifies with increasing strain and decreasing temperature, accompanied by earlier and more rapid damage development at low temperature. Strain–damage correspondence indicates both Mode-II–dominated and mixed-mode (I/II) intra-ply cracking, while delamination shows a stronger Mode-I contribution but remains mixed-mode. Inter-ply kinematic constraint and shear transfer between adjacent plies with mismatched fibre orientations were directly visualised and characterised under HSR loading, particularly at low temperature. Together with the spatially non-uniform and asynchronous development of local deformation through the laminate thickness, these results highlight substantial departures from the nominal in-plane shear state commonly assumed for uniaxial ±45 ° laminate tests under extreme conditions.

1. Introduction

Carbon-fibre-reinforced polymer (CFRP) has been extensively used in the transport industry, where reducing weight yields direct improvement of energy and cost efficiency. Despite numerous advantages, such as high strength-to-weight ratios, corrosion resistance, and design flexibility [1], the anisotropic architectures of CFRP and the different mechanical, physical, and chemical properties of the components can lead to complex damage mechanisms both internally and on the surface [2]. Under high-strain-rate (HSR) loading and/or low temperatures, the damage in CFRP can propagate rapidly after initiation, causing sudden failure of structures resulting from the time-temperature superposition effects of the polymer matrix [3, 4, 5]. Investigating the micro-scale damage initiation and mechanics of CFRP under HSR loading, particularly in conjunction with temperature-dependent behaviour, is therefore of particular importance [6, 7, 8].

Several existing studies have investigated the micro-scale damage mechanisms of continuous fibre-reinforced polymer (FRP) composites under different loading configurations. Damage was found to initiate in the form of micro-cracks and fibre micro-kinking when the continuous FRP is under compression [9, 10, 11]. In tensile tests, fibre breaking, debonding, and pull-out are commonly observed on top of matrix damage [12, 13, 14, 15]. Similar damage characteristics have also been reported in composite tubular structures and hybrid laminates [16, 17, 18]. For laminates loaded off-axis, such as angle-ply (AP) FRP (± 45 °), fibre reorientation is usually induced under both tensile and compressive load, which could considerably alter the stress state, especially in large deformation stages [19, 20]. Furthermore, under bending load, in addition to inter-fibre cracking, large-scale damage such as ply delamination could also initiate during the early stages of damage due to the high inter-laminate shear stress [21, 22].

The strain-rate sensitivity of FRP's damage primarily depends on the relative contribution of matrix during loading, since it is significantly more rate-dependant than the fibres in most FRP composites [23, 24, 25]. Earlier matrix cracking can often be seen in FRP composites under impact loading [26]. Compared to damage caused by quasi-static loading, damage produced at HSR compression and tension is more prone to concentrate at or near the loading surface [27, 28, 29]. Under dynamic bending and shear loading, more fibre fractures can be observed in contrast to quasi-static loading [30]. Ballistic impact can also result in matrix cracking and ply delamination in FRP [31]. However, its failure is, in essence, dominated by fibre shear and tensile failure [32].

Although investigations of FRP's HSR damage mechanisms at varying temperatures are limited, most existing studies agree that both high and low temperatures can weaken the overall performance of FRP composites, albeit through different mechanisms, especially when the matrix plays an important role [33, 34]. As a result of polymers' temperature sensitivity, high temperatures tend to diminish the matrix strength and fibre/matrix bonding at the interfaces, whereas polymer embrittlement at low temperatures impairs the overall energy absorption of composites under loading [35, 36, 37, 38]. For example, a transition in damage mechanism (reduced matrix cracking but increased fibre/matrix debonding) was observed in ±45 ° FRP laminates when the test temperature was changed from low to high [39].

FRP laminates are naturally suitable for performing digital volumetric correlation (DVC) following *in-situ* X-ray computed tomography (CT) by virtue of their high fibre packing density [40, 41, 42]. While the combination of *in-situ* CT and DVC has been widely adopted in quasi-static testing [43, 44, 45, 46, 47], the three-dimensional (3D)

*Corresponding author
ORCID(s):

characterisation of internal damage and micro-mechanics at HSR loading is still a challenge. Investigations of damage mechanisms at HSR loading in existing research mainly rely on post-mortem inspections [48, 49]. A previous study [50] observed rapid subsurface damage initiation and evolution in CFRP *in situ* under low-temperature impact at the meso-scale using X-ray phase-contrast imaging (XPCI), but damage characterisation was limited by available spatial resolution and the 2D nature of the XPCI technique. Under similar testing conditions, a follow-up study quantitatively analysed opened damage (i.e., damage that contains internal void regions) in CFRP laminates using micro-computed tomography (μ-CT) at intermediate-to-late loading stages using conventional image processing techniques [51]. However, the mechanisms of microscopic damage inception under HSR impact and varying temperatures, particularly the coupling between local strain localisation and ultra-fine ply cracking at early loading stages, have not yet been quantitatively resolved.

Therefore, utilising the datasets of the experimental campaign reported in our previous study [51], which focused on opened damage at intermediate-to-late loading stages, the present study shifts the analysis to early-stage damage and introduces a fundamentally different framework by incorporating pre-loading μ-CT scans and applying a dedicated DVC-based approach to resolve microscopic strain–damage interactions. The loading was interrupted at predefined strain levels to preserve early-stage damage. Through DVC-enabled volumetric registration, this approach enables (i) segmentation of micron-scale cracks (2 – 4 μm), (ii) computation of high-resolution microscopic strain fields over sub-volumes ($\sim 16.8 \times 16.8 \times 16.8$ μm^3), and (iii) direct correlation between strain localisation and crack initiation. This integrated strain–damage analysis within a unified volumetric framework provides unique mechanistic insights into early-stage damage evolution as functions of strain and temperature, which were not accessible through conventional experiment, imaging, and post-processing protocols under HSR loading.

2. Materials and Methodology

2.1. Material

The investigated CFRP laminates embedded "standard modulus" carbon fibres (Toray Industries, Inc.) in a high-performance epoxy resin (Hexcel Corporation) to produce unidirectional (UD) fibre/epoxy prepregs. The laminates were manufactured by laying up 16 layers of the UD prepregs following the stacking sequence of $[+45/-45]_{4s}$ and resulting in a fibre volume fraction of around 60 % (calculated from fibre/matrix weight fractions and constituent densities provided by the suppliers, and independently verified by μ-CT image segmentation), as illustrated in Fig.1a. The $[+45/-45]$ laminate configuration was selected as a representative in-plane off-fibre-axis loading scenario. Unlike UD laminates, its dual fibre-orientation architecture enables direct investigation of inter-ply interactions between plies with different fibre directions. At the same time, compared to quasi-isotropic (QI) laminates, the $[+45/-45]$ configuration promotes clearer localisation of internal stress and strain, thereby facilitating high-quality data acquisition and analysis under off-fibre-axis and shear-dominated loading conditions. Under quasi-static loading (approximately at $\dot{\varepsilon} = 3.3 \times 10^{-1}$ s^{-1}), the in-plane shear strength (τ_{21}) and shear modulus (G_{21}) of the CFRP laminate were measured as 82.6 MPa and 2.96 GPa, respectively. The curing process was implemented using an autoclave machine, which raised the temperature to 180 °C at a rate of 1-2 °C min^{-1}, held for 120 min, and then reduced to room temperature at a rate of 2-5 °C min^{-1}. The produced 3 mm thick CFRP panels were then cut into $3 \times 3 \times 3$ mm^3 for HSR testing and μ-CT scanning. This specimen size was selected to satisfy the requirements of full-field synchrotron μ-CT imaging and sufficient voxel resolution for DVC analysis, while ensuring stable dynamic testing conditions.

2.2. Loading and temperature

HSR compression was performed using a split-Hopkinson pressure bar (SHPB) system along the laminate in-plane direction (Fig.1b). This SHPB system was configured with a set of half-inch (about 12.7 mm) Ti-6Al-4V titanium alloy bars with lengths of 200, 1300, and 1100 mm for the striker, input and output bars, respectively. Two sets of strain gauges were mounted on the bars, one at 550 mm distance from the input-bar/specimen interface and the other at 500 mm distance from the output-bar/specimen interface. Two 3 mm-thick Ti-6Al-4V loading platens were used at the bar/specimen interfaces to protect the bar ends from being damaged by the specimens. Secondary loading was prevented by implementing a momentum trap on the input bar so that the recovered specimens only contain damage imposed by a single compression event.

A strain interruption technique was employed to impose different levels of deformation and damage to the specimens. This was achieved by installing precision-manufactured strain control collars at the interface between the output bar and the specimens, as shown in Fig.1c. Collar spacers of different thicknesses were manufactured and subsequently hand-polished to achieve a dimensional tolerance of ± 3 μm. Once the length of the specimens has been compressed to the same level as the thickness of the collar spacers, the input bar end and the collars will come into direct contact and produce a "sudden stop" to the specimen deformation. The target interruption strains (ε_{interr}) were designed in accordance with the non-interrupted response of the specimens tested under similar conditions [51]. The impact velocity of the striker bar was ∼13.8 m s^{-1}, yielding an engineering strain rate of ∼2500 s^{-1} onto 3 mm long specimens. In addition to strain-gauge measurements, a high-speed camera was synchronised with loading to record deformation images *in situ* and directly deduce the specimen ε_{interr} by two-dimensional (2D) digital image correlation (DIC).

The tests were conducted at 23 °C and −50 °C (± 2 °C) to study the role of temperature in the damage mechanisms at

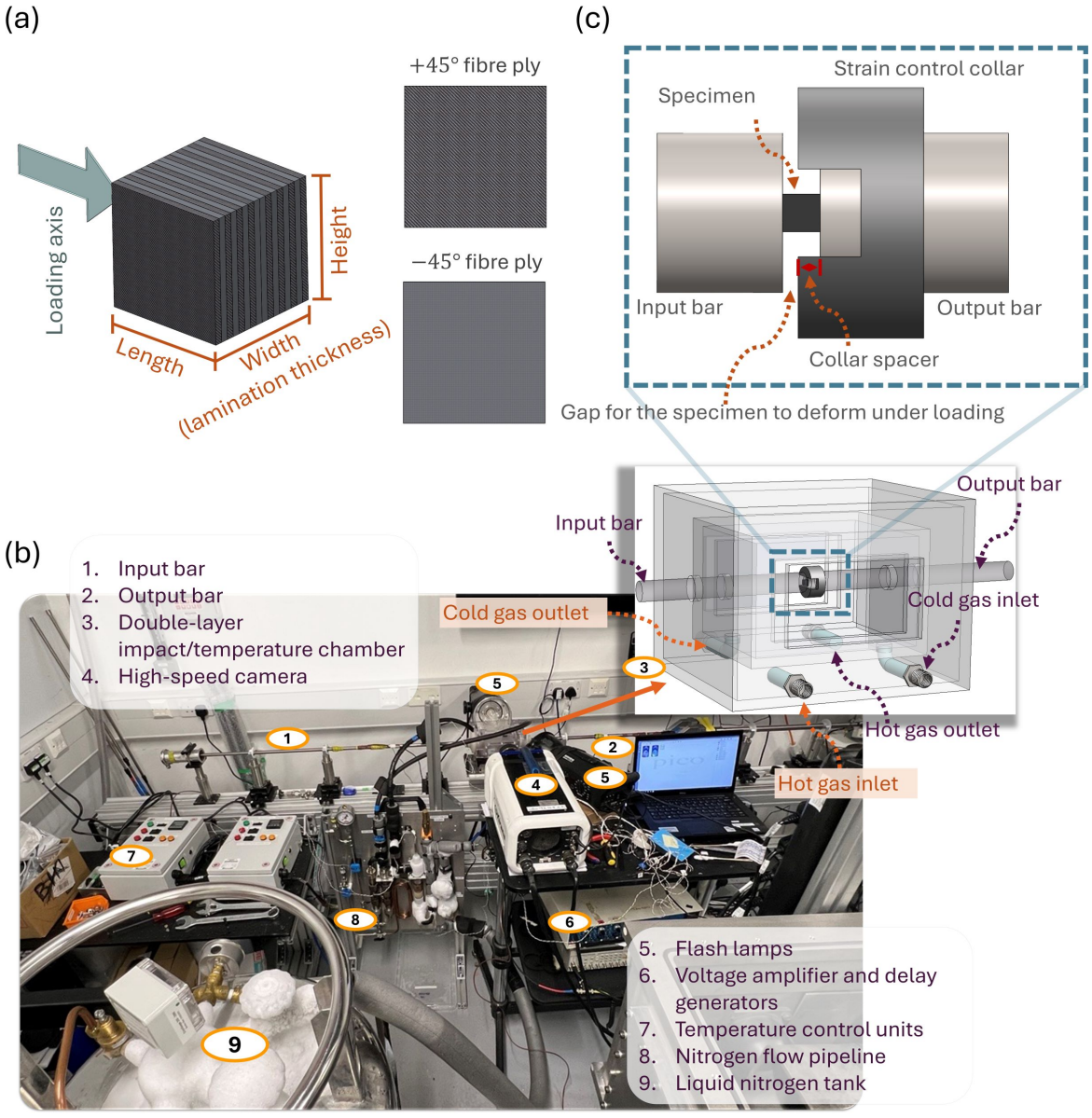

Figure 1: Schematic of the specimens, loading, temperature control, and imaging setups. (a) The specimen geometry formed by stacking plies with +45 and −45 ° fibre pies, (b) a SHPB loading platform mounted with high-speed imaging and temperature control systems, and (c) the zoom-in views of the double-layer impact/temperature chamber and the strain interruption setup.

high rates. The −50 °C condition represents typical ambient temperatures encountered at civil aircraft cruising altitudes and is particularly relevant given the increased brittleness of typical epoxy matrix in the temperature range associated with β-relaxation [52]. The initial temperature was achieved through a bespoke temperature control system for HSR SHPB testing. The cool nitrogen gas originating from an LN2 dewar was heated, regulated and injected into a double-walled impact/temperature chamber (Fig.1c) as both a cooling and heating agent. During the experiment, the inner chamber was maintained at the target testing temperature; meanwhile, the outer "isolation" chamber was heated to prevent moisture and frost from forming on the observation windows. More details on HSR loading, strain interruption, and temperature control setups can be found in previous research [51].

2.3. X-ray imaging strategy

The internal structures of the laminate specimens were examined with synchrotron-based phase-contrast µ-CT on Beamline ID19 at the European Synchrotron Radiation Facility (ESRF). The high photon flux and small effective X-ray source size enable rapid scanning at high spatial resolution (effective pixel size of 2.1 µm × 2.1 µm in this study) while providing propagation-based phase-contrast enhancement [53]. Compared with absorption-contrast imaging alone, phase-contrast propagation improves the visibility of weakly absorbing features and interfaces, facilitating micron-scale

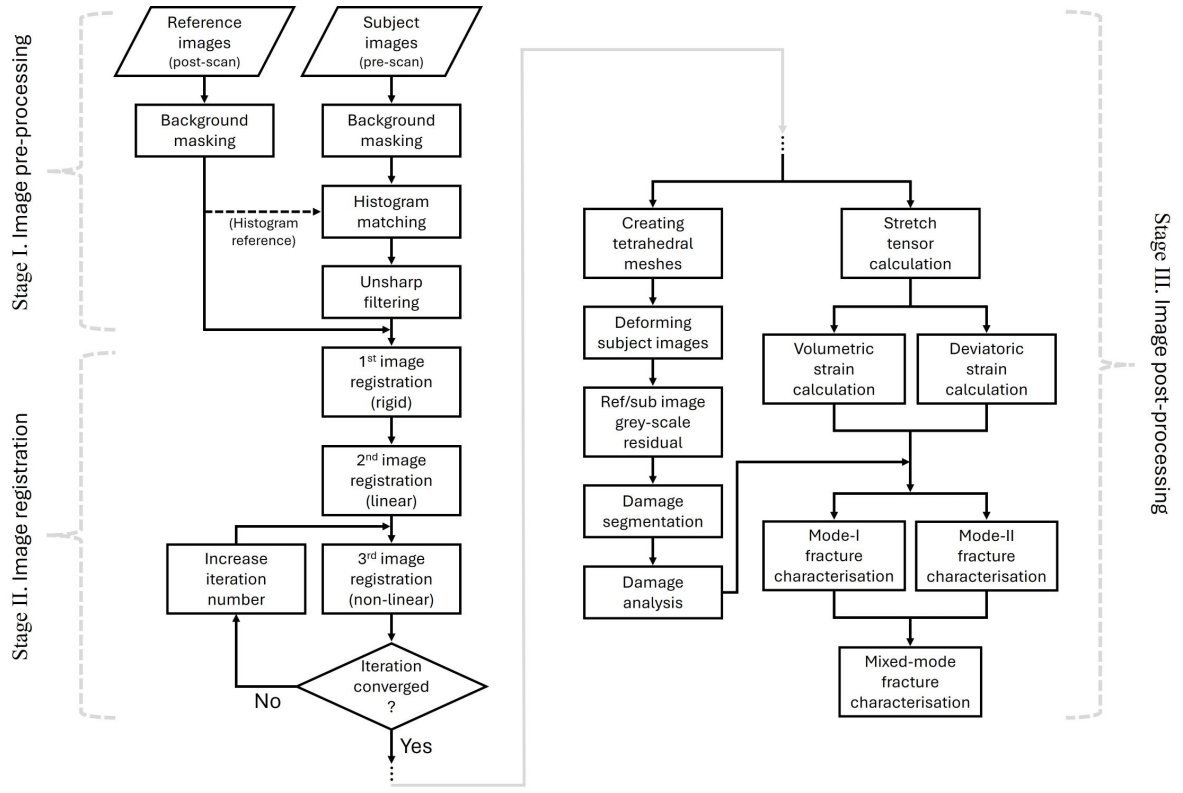

Figure 2: Data acquisition, image processing, damage segmentation, and micro-mechanics analysis flowchart. Stage I involved histogram matching of the subject scans to the reference scans prior to image registration. These pre-processing steps improved grey-scale consistency and ensured robust correlation and numerical convergence. At Stage II, image registration was conducted in three steps (rigid, linear, and non-linear) to achieve correlation from coarse to fine. Stage III performed damage segmentation and strain calculation, which, in combination, help characterise the micro-mechanics of the segmented damage.

damage detection. Based on the phase-contrast tomograms, DVC was applied to quantify loading-induced permanent deformation by correlating volume pairs acquired before loading (pre-scan) and after loading (post-scan) at selected loading stages. The resulting 3D displacement field was then used for micro-scale image registration, enabling accurate voxel-wise comparison between scans, and robust extraction and analysis of both residual strain and micron-scale damage. This analysis pipeline will be discussed in detail in the following sections.

For each experimental condition (interruption strain level and temperature), one specimen was analysed using the full DVC workflow. This was constrained by the requirement of paired pre- and post-loading synchrotron μ-CT scans and the limited availability of beamtime. Mechanical repeatability was verified through multiple SHPB tests under identical conditions, and additional specimens characterised by post-scans exhibited consistent damage morphology and evolution trends. For a given temperature, the physically coherent evolution of global response, damage morphology, and local strain localisation across increasing interruption strain levels further supports the mechanistic consistency of the observed damage processes.

2.4. Image pre-processing

The methodology for image processing and damage analysis in HSR loading testing is presented in Fig.2. Due to the much longer acquisition time relative to the loading event, X-ray tomography cannot be carried out continuously, as in the case of quasi-static tests. However, scanning specimens at separate times (pre- and post-scans) can lead to dissimilarities that originate from fine differences in the X-ray beam and imaging parameters. Thus, prior to image registration, image normalisation was necessary to compensate for differences encountered during post-scans, as shown in Fig.2, Stage I. During this process, post-scans (images of damaged specimens) were selected as references to avoid distortion of the damage features. High-accuracy boundary detection and specimen/background segmentation are required for full-field damage visualisation and characterisation, enabling the study of boundary effects in AP laminates. This was achieved by creating region of interest (RoI) masks using a deep-learning model based on the U-Net architecture integrated in the `Dragonfly 3D World` software [54]. Next, histograms of pre- and post-scans were matched, and an unsharp masking was applied to help minimise the difference in intensity gradients between the two sets of scans. These image pre-processing procedures can effectively enhance gradient-based feature recognition, resulting

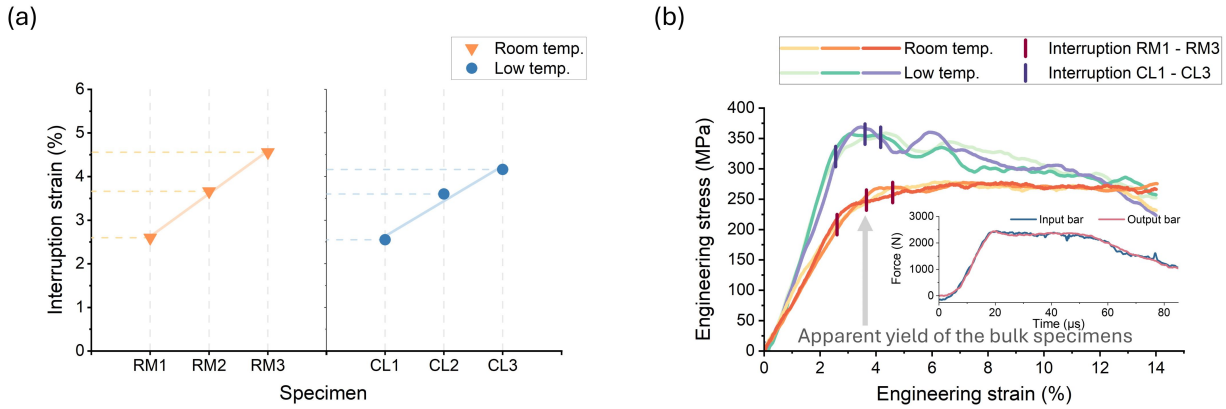

Figure 3: Interruption strain levels for the specimens. (a) The measured strain levels at interruptions show a gradually increasing trend from RM1 to RM3 and from CL1 to CL3. (b) The loading stages of the specimens at the interrupted strain levels are demonstrated, in comparison with the non-interrupted stress-strain curves of the same CFRP laminates tested under similar loading conditions [51]. For clarity, only the pre-failure regime of the stress–strain response is displayed; catastrophic failure of the room-temperature specimens occurs at larger strains. The curves are shown in engineering form (axial engineering strain) and used to mark interruption stages rather than to present converted in-plane shear constitutive data. A representative input and output force–time history from a non-interrupted test is shown in the inset. The forces are in close agreement prior to peak stress, demonstrating dynamic stress equilibrium during SHPB loading.

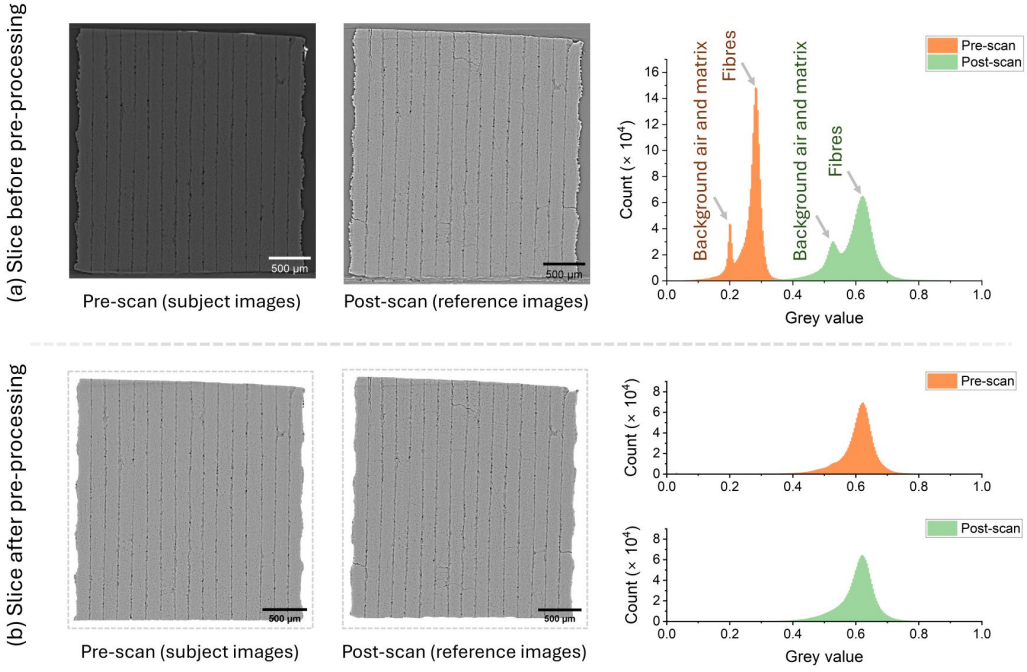

Figure 4: Image pre-processing results. (a) The X-ray μ-CT slices and their histograms of specimen CL2 before and after loading. (b) The same X-ray μ-CT slices and their histograms after the pre-processing. It can be seen that the image background has been removed, and the grey-scale distribution of the slices has been matched. The grey-scale gradients between features are in a comparable state across pre- and post-scans.

in good calculation convergence and less computational cost.

2.5. Image registration

The spatial correspondence between the two tomography datasets was then established through image registration and transformation (Fig.2, Stage II). First, a rigid image transformation (the 1st image registration) was performed in `3D Slicer` [55] to eliminate large-scale specimen misalignment, which, if present, would substantially increase computational cost and reduce robustness during subsequent registration. The 2nd image registration applied a global linear (affine) coordinate transformation to the subject volumes using the `SPAM` analysis toolkit [56], following,

$$\mathbf{X}' = \mathbf{F}\mathbf{X} + \mathbf{t}, \tag{1}$$

where $\mathbf{X}'$ and $\mathbf{X}$ denote the voxel coordinates in the reference volumes and the subject volumes, respectively ($\mathbf{X}'$, $\mathbf{X} \in \mathbb{R}^3$). $\mathbf{F} \in \mathbb{R}^{3\times3}$ stands for the transformation (deformation) gradient tensor, and $\mathbf{t} \in \mathbb{R}^3$ is the translation vector [57]. The assembled linear deformation matrix $\boldsymbol{\phi}$ is written in homogeneous coordinates ($\mathbf{X}_h = [\mathbf{X}^\mathsf{T}\ 1]^\mathsf{T}$) as,

$$\boldsymbol{\phi} = \begin{bmatrix} F_{xx} & F_{xy} & F_{xz} & t_x \\ F_{yx} & F_{yy} & F_{yz} & t_y \\ F_{zx} & F_{zy} & F_{zz} & t_z \\ 0 & 0 & 0 & 1 \end{bmatrix}, \tag{2}$$

such that the transformation can be written explicitly as

$$\begin{bmatrix} X'_x \\ X'_y \\ X'_z \\ 1 \end{bmatrix} = \begin{bmatrix} F_{xx} & F_{xy} & F_{xz} & t_x \\ F_{yx} & F_{yy} & F_{yz} & t_y \\ F_{zx} & F_{zy} & F_{zz} & t_z \\ 0 & 0 & 0 & 1 \end{bmatrix} \begin{bmatrix} X_x \\ X_y \\ X_z \\ 1 \end{bmatrix}. \tag{3}$$

With the obtained ϕ as an initial guess, the 3rd image registration correlated the reference and subject volumes within local regions by segmenting the volumes using structured grids and solving the non-rigid transformation fields. This was achieved by minimising an error function $\mathcal{T}(\phi)$ defined over a correlation sub-volume $\mathbf{\Omega_s}$ in the reference volume,

$$\mathcal{T}(\phi) = \tfrac{1}{2} \sum_{\mathbf{X}' \in \mathbf{\Omega_s}} \left[T(\mathbf{X}') - I\left(\phi^{-1}(\mathbf{X}')\right) \right]^2, \tag{4}$$

where $T(\mathbf{X}')$ denotes the voxel intensity of the reference evaluated at coordinate $\mathbf{X}'$, and $I(\cdot)$ represents the voxel intensity of the subject evaluated at the mapped coordinates. The optimal transformation parameters were obtained by iteratively updating $\boldsymbol{\phi}$ such that,

$$\frac{\partial \mathcal{T}}{\partial \boldsymbol{\phi}} = \mathbf{0}, \tag{5}$$

which was solved using a Newton-Raphson optimisation until the norm of the gradient $\nabla\mathcal{T}(\boldsymbol{\phi})$ falls below the prescribed convergence threshold (0.01 in the present calculation).

A hierarchical coarse-to-fine strategy was adopted to improve convergence robustness. The DVC computation started with a coarse correlation sub-volume and progressively refined the solution using smaller window sizes, each iteration building upon the previously obtained transformation field. Specifically, the sub-volume size was reduced from 64×64×64 voxels to 8×8×8 voxels, with a decrement of 4 voxels per iteration.

2.6. Image post-processing and analysis

The local transformations derived from the preceding image registration were then input into two analysis tracks - damage segmentation and strain calculation, as illustrated in Fig.2, Stage III. Tetrahedral meshes were generated to discretise the subject volumes. Local transformations obtained from DVC analysis were applied to these meshes, allowing consistent deformation of the subject volumes with respect to the measured displacement fields [56]. This enabled accurate mapping of the subject volumes onto the reference volumes, providing the basis for subsequent damage segmentation. Next, both deformed and undeformed subject volumes were subtracted from the reference volumes to calculate the grey-scale residuals r_{def} and r_{undef}, respectively, following,

$$\mathbf{r_{def}} = \mathbf{I_{ref}} - \mathbf{I^{def}_{obj}}, \tag{6}$$

$$\mathbf{r_{undef}} = \mathbf{I_{ref}} - \mathbf{I_{obj}}, \tag{7}$$

where $\mathbf{I_{ref}}$ is the reference volumes (post-scans). $\mathbf{I_{obj}}$ and $\mathbf{I^{def}_{obj}}$ denote the object volumes (pre-scans) before and after deformation according to the obtained transformations, respectively. Subsequently, the standard deviation (**STD**) for r_{def} and r_{undef} can be calculated to assess the effectiveness of DVC analysis using,

$$\mathbf{STD} = \sqrt{\frac{1}{N}\sum_{i=1}^{N}(x_i - \mu)^2}, \tag{8}$$

where N and μ represent the total number of voxels and the mean intensity in the computing volumes, x_i is the intensity of each voxels. The resulting r_{def} can also be used to highlight the structural differences between $\mathbf{I_{ref}}$ and $\mathbf{I^{def}_{obj}}$ (e.g., cracks generated during loading). From there, micron-scale crack segmentation can be accomplished using maximum entropy image thresholding to create damage masks for qualitative and quantitative analysis. Visualisation and analysis of local residual displacement, strain concentration, and micron-scale damage were performed through the combined use of `Dragonfly 3D World` [54], `ImageJ` [58], `ParaView` [59], and developed `Python` scripts.

In the strain calculation, microscopic local strain was computed directly from the transformation matrix for each sub-volume ($8 \times 8 \times 8$ voxels, approximately $16.8 \times 16.8 \times 16.8$ μm^3) on the structured grid. The local deformation gradient $\mathbf{F}$ was obtained by linking eight neighbouring grid nodes [56], following,

$$\mathbf{F} = \mathbf{I} + \frac{d\mathbf{u}}{d\mathbf{X}'}, \tag{9}$$

where $\mathbf{I}$ is the identity matrix, and $\nabla\mathbf{u}$ denotes the gradient of the displacement tensor. The right stretch tensor $\mathbf{U}$ was derived using polar decomposition [60], expressed as,

$$\mathbf{F} = \mathbf{R}\mathbf{U}, \tag{10}$$

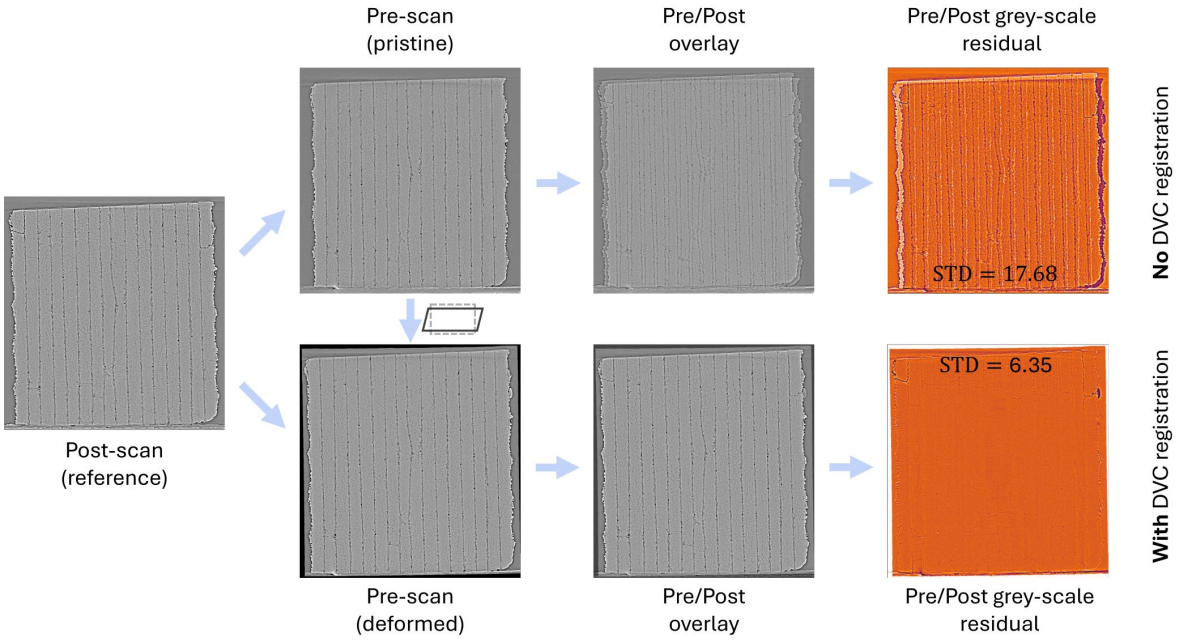

Figure 5: Image registration before (top row) and after (bottom row) DVC. Image overlay and subtraction results are displayed to demonstrate the feature matching between pre- and post-scans. A good match can be found after performing DVC, evidenced by a clearer overlay image result and significantly homogenised (reduced STD) grey-scale residuals.

$$\mathbf{U} = (\mathbf{F}^{\mathsf{T}}\mathbf{F})^{1/2}, \tag{11}$$

where $\mathbf{R}$ is a proper orthogonal rotation ($\mathbf{R}^{\mathsf{T}}\mathbf{R} = \mathbf{I}$, $\det \mathbf{R} = +1$). The stretch tensor can be multiplicatively decomposed into an isotropic and a deviatoric part as,

$$\mathbf{U} = \mathbf{U}_{iso} \cdot \mathbf{U}_{dev}, \tag{12}$$

where $\mathbf{U}_{\text{iso}} = J^{1/3}\mathbf{I}$ represents the volumetric stretch associated with the local volume change $J = \det(\mathbf{F})$, and $\mathbf{U}_{\text{dev}} = J^{-1/3}\mathbf{U}$ captures the isochoric (shape-changing) deformation. Volumetric and deviatoric deformation measures were analysed together with the segmented damage, as they highlight different deformation modes and therefore different damage mechanisms. In particular, local volumetric expansion is indicative of opening-dominated processes (Mode I), whereas deviatoric deformation and shear localisation are commonly associated with sliding-dominated mechanisms (Mode II).

3. Results and discussion

3.1. Interrupted strain comparison

The interrupted strain levels achieved in both room- and low-temperature specimens are shown in Fig.3a, increasing from $\sim$ 2.5% to 4.5% for subsequent specimens (i.e., RM1 to RM3, CL1 to CL3). The relative global stress-strain stages of the specimens at the interruption points can be evaluated by comparing with the non-interrupted responses obtained from similar loading and environmental conditions, as presented in Fig.3b. It should be noted that the stress–strain curves are presented in engineering form. As the maximum deformation remains below 5% in all interruption cases, engineering strain, which is commonly adopted in ± 45 ° laminate testing in accordance with ASTM D3518/D3518M [61], is considered appropriate. Within this small deformation range, the difference between engineering and true strain measures is negligible for the purposes of the present damage and strain localisation analysis. The interrupted strain level was acquired from direct displacement measurement using DIC, the detailed analysis of which is discussed in the previous study [51]. The strain of the specimens (RM1 – RM3 at room temperature and CL1 – CL3 at low temperature) was interrupted in the vicinity of the apparent yield, allowing the study of the microscopic damage evolution throughout the critical transition from nominal elastic to inelastic bulk deformation regimes.

3.2. Pre-processed image analysis

The same specimen scanned at separate times on the same synchrotron beamline can possess different grey-scale distributions and gradients, as shown in the X-ray µ-CT slices in Fig.4a. The grey scale of the empty region (the air), the specimen resting platform, and the resin-rich regions are intertwined, because of the low X-ray absorption of the epoxy matrix and the presence of phase-contrast effects. For each of the histograms, the left-side peak (the relatively lower one), together with its base, is a composition of these three components, making the background (the air and platform) difficult to subtract using a thresholding

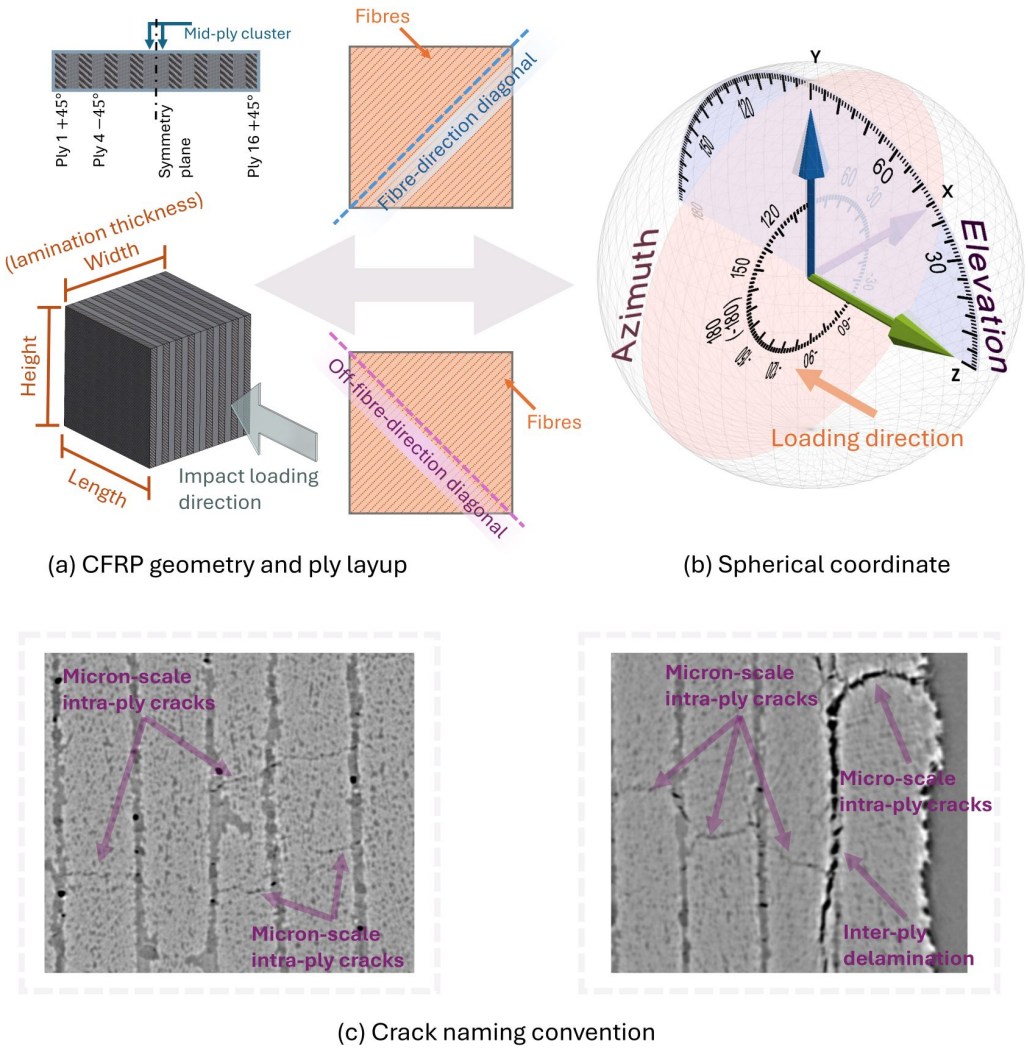

(a) CFRP geometry and ply layup

(b) Spherical coordinate

(c) Crack naming convention

Figure 6: Notation and coordination systems used in analysis. (a) The geometry and ply layup of the CFRP laminates are demonstrated, together with the illustration of two types of diagonals that are used in the damage micro-mechanics discussion. (b) The 3D spherical coordinate system is used to indicate the direction of displacement vectors in a 3D space. (c) The naming convention for different damage morphologies.

method. The use of a bespoke `Python` code and a U-Net-based deep-learning algorithm (integrated in `Dragonfly 3D World`) enabled the accurate removal of the background (see the no background slices and single-peak histograms in Fig.4b) through edge, gradient, and texture detection. Hence, the registration, analysis, and visualisation of the images in later stages would not include the background regions.

After removing the background, discrepancies in the histograms between the pre- and post-scans were still evident (Fig.4a). Given that this DVC analysis was a grey-scale gradient-based calculation, comparable distributions and contrast were needed for good convergence and feature registration. Therefore, the pre-scan histogram was matched (cumulative histogram mapping) to the post-scan histogram, and unsharp filtering was applied. Fig.4b displays the same X-ray radiography slices as in Fig.4. The histograms of the two slices, one from the pre-scan and the other from the post-scan, exhibit highly comparable structures and grey scales, meaning that the gradient differences between the components, such as the voids, matrix, and fibres, in these pre- and post-scan slices have been matched.

3.3. Image registration effectiveness

The image registration processes performed in the present research are essential for identifying fine cracks and other microscopic damage signatures, such as deformation. Fig.5 showcases the effectiveness of image registration between the pre- and post-scans. Overlay and subtraction between unaltered pre- and post-scan slices demonstrate clear misalignment, particularly recognisable at the specimen's edges (top-row images in Fig.5). However, after being deformed through image registration, the pre-scan (50% opacity) became barely visible when overlaid on the post-scan. A substantial reduction in grey-scale residuals can be found in the subtraction image with a drop in STD from 17.68 to 6.35, indicating a significantly higher degree of comparability

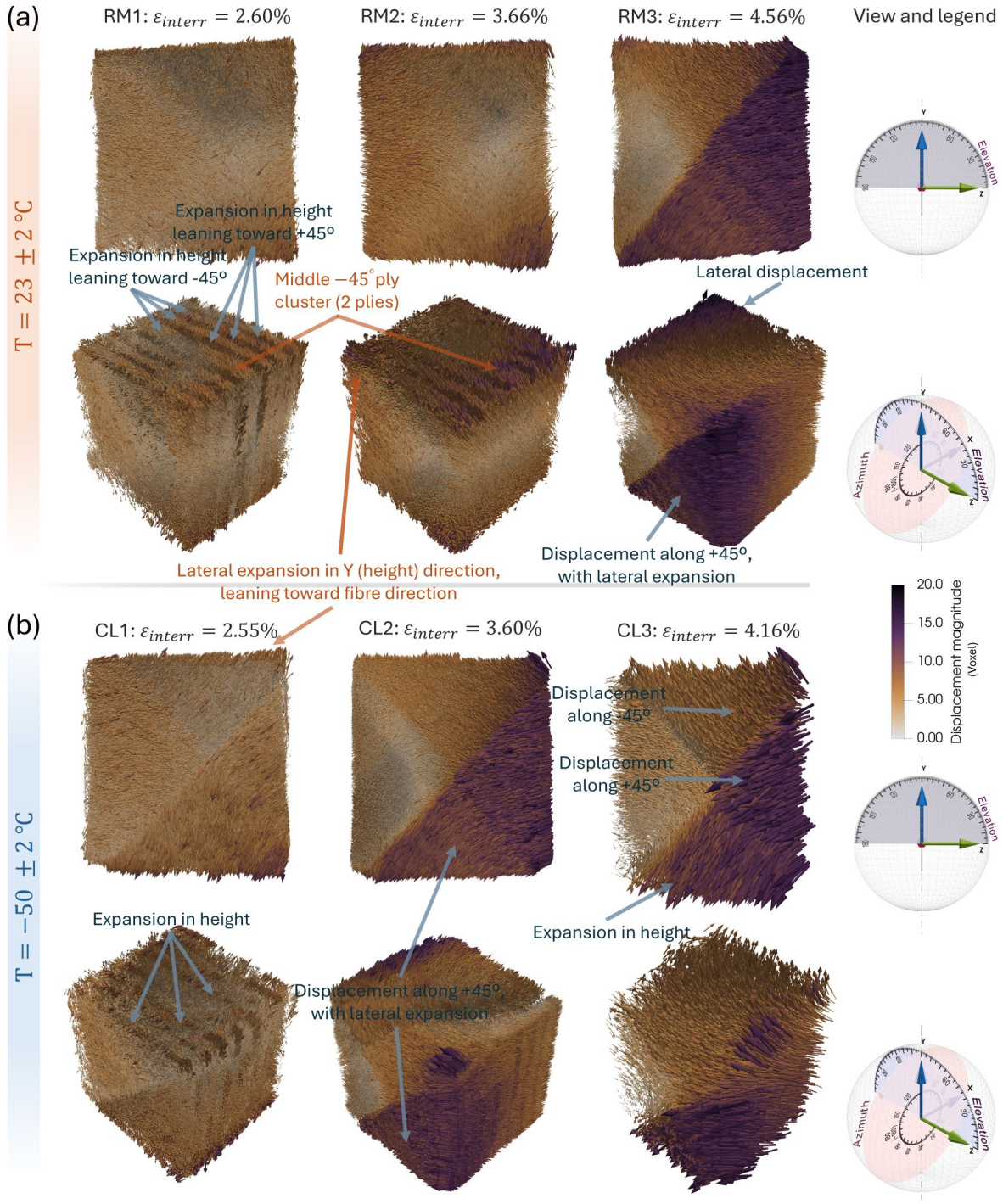

Figure 7: 3D microscopic displacement vectors calculated from DVC for specimens at (a) room and (b) low temperatures. Two views are presented for each specimen. The directions of the displacement vectors are consistent with the arrow directions, and the colour code and the length of the arrows indicate their magnitude. Prominent directionality is observed in the specimens at both temperatures, with the low-temperature ones being more pronounced at similar strains. An evident correlation between displacement direction and fibre/ply arrangement is visualised. More direction indications can be found in Fig.6.

between the post-scan and the deformed pre-scan (bottom-row images in Fig.5).

The notation, coordinate, and naming conventions used in the data analysis are specified in Fig.6, in which Fig.6a shows the dimension notation and ply layup of the CFRP specimens. Fig.6b is the spherical coordinate system adopted in the displacement vector analysis. The XY plane is parallel to the impact face of the specimens, and the loading was applied along the Z axis towards the −Z direction. The naming of cracks with different morphologies is illustrated

in Fig.6c. Intra-ply cracks that are shown to be 1 to 2 pixels in width were named as micron-scale intra-ply cracks, while wider ones with obvious internal void space between the edges were labelled as opened cracks. In addition, inter-ply delamination is the separation of two adjacent plies in the resin-rich regions.

3.4. Micro-scale displacement analysis

Specimen internal displacements produced from the DVC analysis are demonstrated in Fig.7. The arrows point to the displacement directions, and the magnitude of the displacement is indicated by the length and colour map. For each specimen, two views – front (YZ plane) and isometric – are presented. It can be seen that at equivalent strain levels (each column in Fig.7), the specimens tested at low temperature exhibit earlier and larger displacements with greater localisation. The internal local displacements of the specimens show a strong directional feature influenced by the internal structures of the laminates, mainly the fibre directions and the ply stacking sequence. This directional feature is more evident in specimens with larger interrupted strains or at similar strains but lower temperatures. Large surface ply displacement (above 10 voxels) along the fibre direction (+45°) can be found in RM3, CL2 and CL3, identified by arrows with longer length and darker colours. For specimens with small interrupted strains, such as RM1, RM2, and CL1, lateral expansion in the Y direction (the height direction of the specimens) is prominent with inclinations towards the fibre directions in individual plies.

The statistical analysis of the vector direction and magnitude is presented in Fig.8. For each specimen, three plots were produced based on displacement vectors – direction histogram (DH), accumulated magnitude histogram with normalised colourmap (AMH-NC), and accumulated magnitude histogram with fixed-range colourmap (AMH-FC). The DH plots illustrate the distribution of vector directions in each specimen. In the AMH-NC plots, the magnitude of each displacement vector is accumulated within each direction bin, enabling visualisation of the accumulated vector magnitude in different directions using a colour map normalised to the maximum and minimum values in the volume. This representation facilitates the assessment of the alignment between the direction and magnitude distributions. For instance, an overall flattening of the intensity distribution from DH to AMH-NC (i.e., a higher degree of spatial uniformity in AMH-NC compared to DH) can indicate a mismatch of the peak intensity between the direction and magnitude distribution. Lastly, the AMH-FC plots employ a fixed colour scale, allowing direct and consistent comparisons of accumulated vector magnitudes across specimens.

Interestingly, in specimen RM1, displacement is highly concentrated in the specimen's in-plane direction (length and height). Four labelled high-intensity regions, denoted RM1-1, RM1-2, RM1-3 and RM1-4 in Fig.8, reveal a pronounced tendency for in-plane displacement along the specimen's length and height directions. These displacements lean toward +45 or −45° fibre directions in each ply (also see RM1 in Fig.7). Despite the existence of Poisson's effect, the noticeable specimen expansion in the height direction (90 and −90 °) in this stage is fundamentally induced by the off-fibre-axis loading, which drives ply displacement along +45 or −45 ° fibre directions. The displacement in the specimen width direction remains minimal, as evidenced by the vertically aligned intensity distribution centred at about 90 and −90° in the azimuth [62]. As ε_{interr} increases to 3.66% (RM2), a modest increase in width-direction displacement becomes apparent, as indicated by the higher intensities observed in Zones RM2-1 and RM2-2 when compared to RM1 (Fig. 8). Specimen RM3 represents a further development of this behaviour, characterised by a clear rotation of the dominant displacement direction. Zone RM3-1 exhibits a strong in-plane displacement approximately aligned with the +45° fibre direction, accompanied by an outward component in the specimen width direction (i.e., the −X direction in the global spherical coordinate system). Meanwhile, Zone RM3-2 is approximately the central symmetry of RM3-1, showing a corresponding displacement pattern on the opposite side of the specimen (also see RM3 in Fig.7). Similarly, Zones RM3-3 and RM3-4 describe displacement components that intersect the RM3-1 and RM3-2 directions at approximately 90° in the −45° fibre plies. Owing to the alternating stacking sequence of the +45 and −45° fibre ($[+45/-45]_{4s}$ layup), the inter-ply interaction in orthogonal fibre orientations gives rise to a coherent band of displacement directions, as shown in RM3, Fig.8.

It is notable that, for RM1 and RM2, the AMH-NC plots exhibit a pronounced flattening relative to the corresponding DH plots once the accumulated vector magnitudes are incorporated, whereas the AMH-NC plot for RM3 remains broadly similar to its DH plot. The evident flattening observed in RM1 and RM2 arises from an intensity mismatch between the direction distribution and the magnitude distribution of the displacement vectors. This indicates that, although a large number of vectors in RM1 and RM2 were orientated along similar directions, forming well-defined direction clusters, their magnitudes are relatively small and more spatially dispersed. In other words, at this stage, the localisation of displacement magnitude is markedly weaker than the localisation of displacement direction. In contrast, no pronounced flattening is observed in the AMH-NC plot of RM3 when compared with its DH plot, indicating that, at higher strain levels, the direction distribution is in good agreement with the corresponding magnitude distribution. Furthermore, a clear trend of increasing direction distribution and growing in magnitude with increasing ε_{interr} can be identified in the displacements by cross-comparing RM1, RM2 and RM3 using the AMH-FC plots. This evolution is attributed to the progressive development of volume expansion, contraction, and shear deformation along the three specimen dimensions.

CL1 exhibits the lowest ε_{interr} among low-temperature specimens. While similar in-plane displacement patterns and limited specimen width expansion can be observed, similarly to RM1 and RM2, the displacement of CL1 is

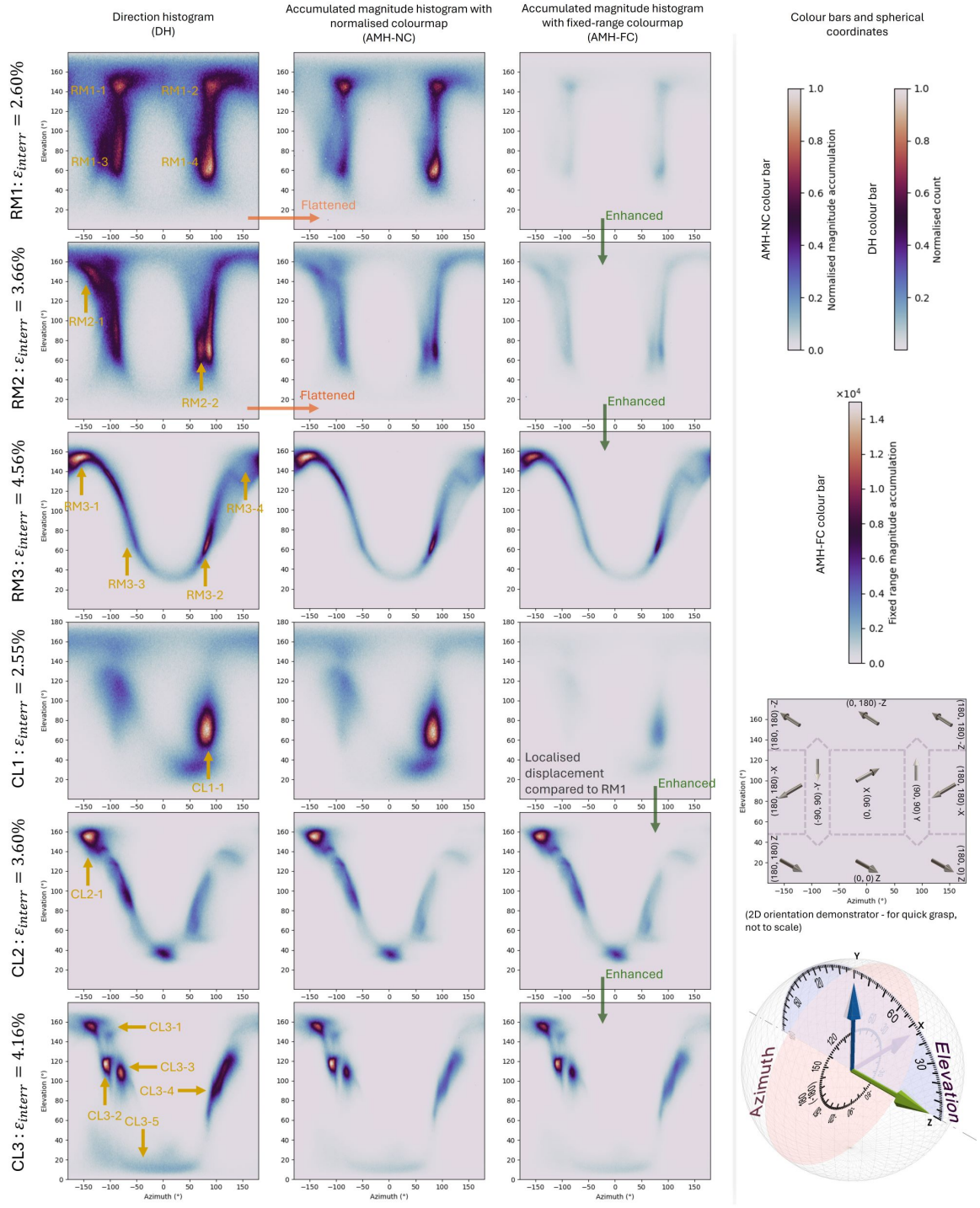

Figure 8: Distribution plots for the direction and magnitude of the microscopic displacement in the specimens. The DH plots demonstrate the direction distribution of the displacement vectors. The AMH-NC plots incorporate the vectors' magnitude into the DH plots to visualise the consistency between the direction and magnitude distributions. The AMH-FC normalise the plots with the same colour scale to form a clear comparison across specimens. The distribution plots should be interpreted in conjunction with the spherical coordinate and 2D demonstrator at the side. More direction indications can be found in Fig.6.

highly localised within Zone CL1-1, as highlighted in Fig.8. This pronounced localisation is indicative of a brittle deformation behaviour under low-temperature conditions [39]. Although CL2 was interrupted at $\varepsilon_{interr} = 3.60\%$, it already demonstrates the formation of a nearly coherent displacement band, comparable to that observed in RM3 at a higher strain level ($\varepsilon_{interr} = 4.56\%$). Nevertheless, the displacement field in CL2 remains more strongly localised than its room-temperature counterpart, observed from the AMH-FC plots.

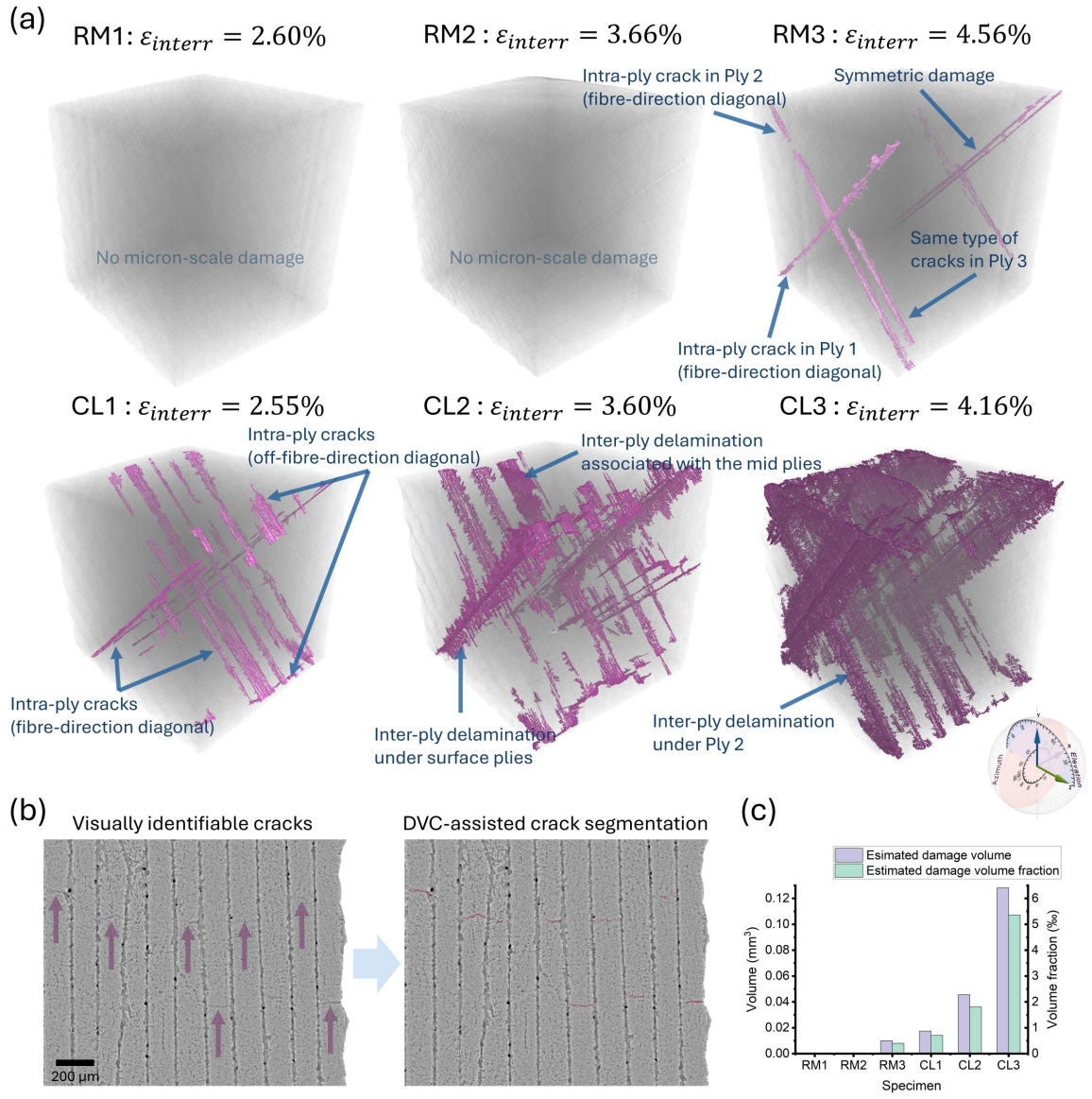

Figure 9: Segmented damage at micron-scale and above in the specimens. (a) The damage segmentation and visualisation show the damage initiation and evolution with increasing axial strain level. [(b) Representative comparison between visually identifiable micron-scale cracks and DVC-assisted crack segmentation on the same μ-CT slice. Arrows indicate cracks identifiable in the raw image, while the red overlays denote the corresponding segmented damage features obtained using the proposed pipeline, demonstrating the consistency between visual inspection and automated detection.] (c) The damage volume statistics of the specimens at different axial strain levels. The quantified damage volume and corresponding volume fraction are influenced by factors such as image acquisition consistency, pre-processing, registration accuracy, and segmentation thresholding. The presented results are therefore intended to illustrate the relative evolution and overall trend of damage growth across different strain levels, rather than to provide absolute volumetric quantification. The proposed experimental and analysis workflow enables high-quality recognition and segmentation of the micron-cracks. Micron-cracks initiate before the apparent yield of the low-temperature specimens and develop significantly more rapidly than the room-temperature specimens.

The DH plot of CL3 shows that the displacement vectors are highly concentrated in four distinct zones, labelled CL3-1, CL3-2, CL3-3 and CL3-4 in Figs.7 and 8 (CL3). Zones CL3-1 to CL3-3 correspond to the displacement vectors influenced predominantly by the +45° fibre direction, whereas the displacement in CL3-4 is approximately aligned with the −45° fibre direction. Moreover, the displacement vectors opposing the loading direction are also observed in CL3 and are labelled Zone CL3-5. This behaviour indicates that the residual deformation along the specimen length direction (i.e., the ± Z axis) in CL3 is significantly larger than that observed at room temperature (RM3).

Similarly to RM3, the AMH-NC plots for CL1 to CL3 show only marginal flattening when compared with the corresponding DH plots, indicating a high degree of consistency between the direction and magnitude distribution of the

displacement vectors. In particular, this consistency emerges at a much lower strain level in low-temperature specimens ($\varepsilon_{interr} = 2.55\%$) than at room temperature, where a comparable behaviour is only observed at 4.56%. This observation further suggests a higher degree of displacement localisation (both in magnitude and direction) in CFRP under low-temperature conditions at a microscopic scale. Meanwhile, the progressively enhanced AMH-FC distributions from CL1 to CL3 reflect the continued development of internal deformation with increasing global strain, following a trend similar to that observed in the room-temperature specimens.

3.5. Micron-scale damage analysis

The spatial distribution, quantity, and propagation characteristics of micron-scale damage within the specimens are presented in Fig.9a, extracted using the image processing workflow proposed in this study. An example 2D slice from specimen CL1 is shown in Fig.9b, revealing the presence of micron-scale cracks (approximately 2–4 pixels in width) and their segmentation. [Given that the detected crack widths approach the effective spatial resolution limit of the μ-CT system, the identification of such fine damage features does not rely solely on conventional grey-level thresholding. Instead, the present approach is based on DVC-assisted registration of paired pre- and post-loading scans, allowing newly formed damage to be identified from structured residuals after deformation compensation. Similar strategies have been adopted in recent studies for resolving fine-scale damage in tested specimens using DVC [42, 43]. In addition, the segmented cracks show clear spatial correspondence with visually identifiable cracks in the raw images (Fig.9b), providing additional independent evidence for the physical relevance of the detected damage features.] Quantitative estimation of damage volume fractions is summarised in Fig.9c to illustrate the progressive growth of damage across the specimens. [These quantities are interpreted as estimated and trend-based metrics rather than absolute volumetric measurements.] The present study focuses on elucidating crack initiation mechanisms through the spatial correlation between damage morphology and microscopic strain localisation. The spatial agreement between the extracted cracks and the independently computed strain fields further supports the reported damage evolution trends.

Despite being subjected to comparable levels of interrupted global strain, the low-temperature specimens exhibit a markedly accelerated development of micron-scale damage compared with their room-temperature counterparts. No resolvable damage is detected in RM1 and RM2, corresponding to stages before and approximately at the global apparent yield, respectively. Micron-scale intra-ply cracks first emerge in the room-temperature specimens when ε_{interr} increases to approximately 4.56% (RM3). These cracks are predominantly confined in a very limited number (two in the present case) of plies underneath the surface ply, aligned with the fibre directions on both sides of the laminate, and concentrated along the fibre-direction diagonals within individual plies (see Fig.6a for ply geometry notation).

In contrast, resolvable cracks are already present in the low-temperature specimens at the lowest interrupted strain level investigated ($\varepsilon_{interr} = 2.55\%$ for CL1), which is prior to the global apparent yield and approximately at the end of the nominal elastic regime, as indicated in Fig. 3b. Although these cracks are very small in width, they are distributed more uniformly across the plies throughout the specimen lamination thickness. Similar enhanced damage distributions in AP CFRP at low temperatures have also been reported under quasi-static loading conditions [39]. The segmented cracks are larger and more contiguous in the two surface plies (Ply 1 and 16) and in the two middle plies (−45° mid-ply cluster – Ply 8 and 9), indicating elevated stress concentrations in these regions. In addition, several discrete intra-ply cracks oriented along the off-fibre-direction diagonals (see Fig.6a for ply geometry notations) are observed near the impact surface. Building upon the crack morphology observed in CL1, specimen CL2 exhibits additional damage in the form of mild inter-ply delamination between Ply 1 and 2, and between Ply 15 and 16, which is spatially connected to the intra-ply cracking in the surface plies. Similar inter-ply delamination is also observed between Ply 7 and 8, linking to intra-ply cracks in the middle plies (Ply 8 and 9). This behaviour suggests that stress redistribution following the onset of intra-ply cracking can promote inter-ply delamination [19]. Damage in CL3 further increases in volume relative to CL2, with inter-ply delamination extending to the interfaces between Ply 2 and 3, and between Ply 14 and 15. This delaminate progression pattern indicates a surface-to-inner propagation trend [51].

3.6. Microscopic strain analysis

The 3D distribution of the local deviatoric and volumetric residual strain within the tested specimens is illustrated in Fig.10. For RM1 and RM2, no evident localisation of either deviatoric or volumetric strain exceeding 5% is observed within the bulk of the specimens. The apparent strain localisation visible near the top surface of the strain fields is attributed to edge correlation artefacts arising from imperfect background removal and edge artefacts in the original X-ray images. Consistent with this observation, no resolvable damage is detected at these stages, as shown in Fig.9a for RM1 and RM2. At room temperature, when ε_{interr} increases to 4.56% (RM3), a pronounced localisation of deviatoric strain emerges within the surface ply. The concentrated deviatoric strain aligns approximately with the local fibre direction and spatially coincides with the intra-ply cracks observed near the fibre-direction diagonal of the ply, as shown for RM3 in Fig.9a. At these regions of damage/strain localisation, the deviatoric strain magnitude is significantly greater than the corresponding volumetric strain, indicating that the associated intra-ply cracking is predominantly shear-dominated. This behaviour is more clearly demonstrated in Fig.11 (a and b).

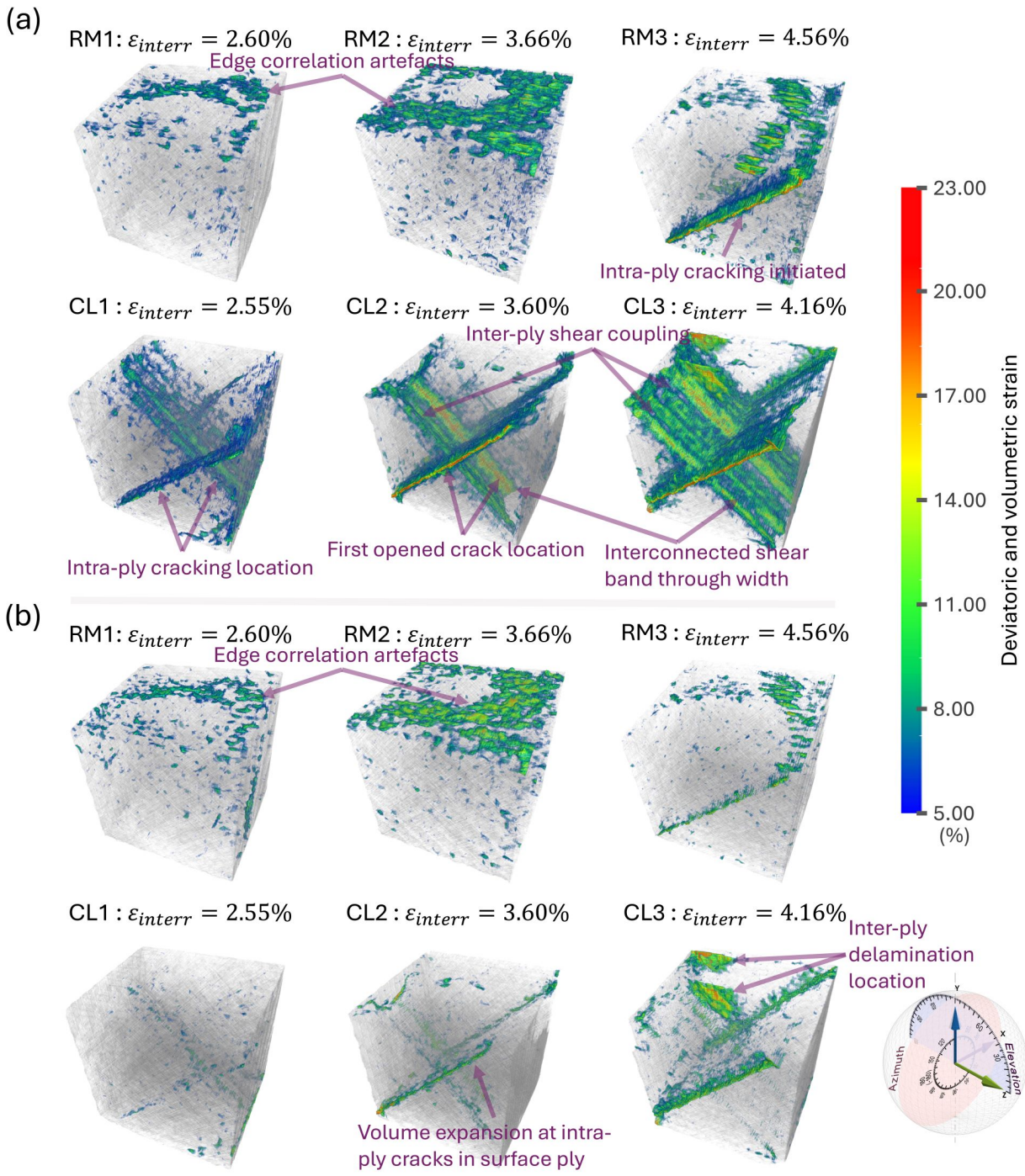

Figure 10: Distribution and intensity of (a) deviatoric and (b) volumetric components in specimen local strain. Both strain components develop more rapidly at low temperatures. The deviatoric strain propagates along the fibre directions, forming shear bands. High volumetric strain is observed between plies in the delamination regions. The location and magnitude of the strain are in good agreement with the segmented damage, which reveals the damage micro-mechanics. Both Mode-II-dominant and mixed-mode fractures are found in intra-ply cracking, whereas ply delamination shows predominantly mixed-mode features, with a notable contribution from volumetric behaviour.

All low-temperature specimens exhibit a pronounced deviatoric deformation behaviour similar to that observed in RM3. Its degree of deviatoric deformation increases progressively from CL1 to CL3, concomitant with the growth of intra-ply damage, as shown in Fig.9a. The highest concentrations of deviatoric strain are located in the surface plies and mid-ply clusters, where opened cracks are first observed. In these damage regions, the deviatoric strain displays both a broader spatial distribution and a higher

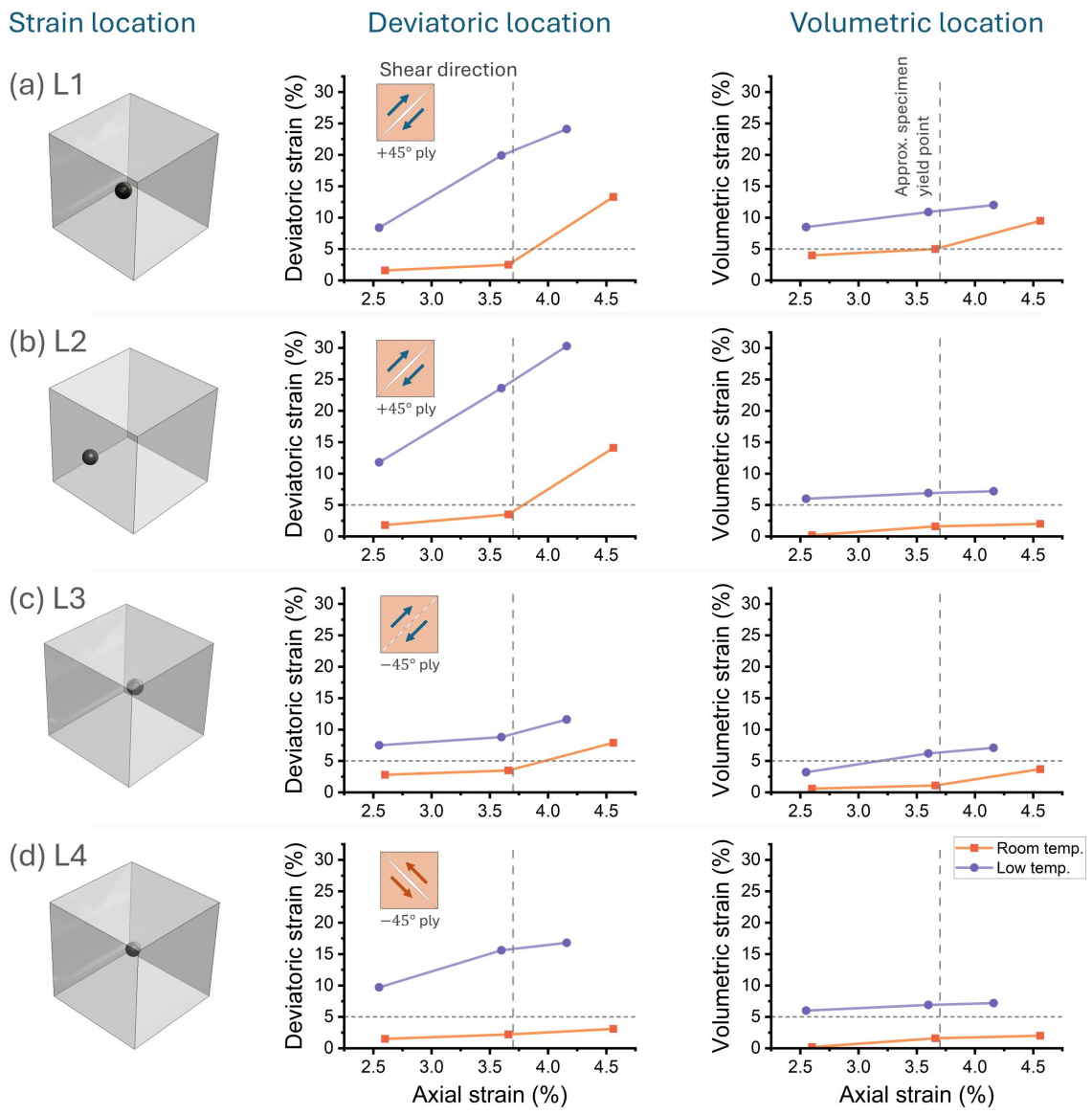

Figure 11: Microscopic strain development at four representative locations: (a) L1, (b) L2, (c) L3, and (d) L4. The deviatoric strain shows a more pronounced increase compared to the volumetric strain, as the selected locations are all on the deviatoric-dominated high-strain bands. L1 and L2 lie in the surface ply (Ply 1 or 16) along the high-strain band, presenting noticeable strain increases with the increasing macroscopic strain. L3 sits at the same ply location as L1 but on the underlying ply (Ply 2 or 15). A clear shear strain localisation can be observed along the off-fibre-direction diagonal of the ply (perpendicular to the fibre direction) at L3, causing inter-ply shear transfer and a contiguous shear band through laminate thickness. L4 represents the increase of the strain propagated along the −45 °C fibre direction in the mid-ply cluster.

intensity. In contrast, at locations dominated by inter-ply delamination in CL3, volumetric strain becomes comparatively more pronounced, indicating that volumetric deformation plays a more significant role in the delamination process. Combined with the inter-ply shear induced by excessive intra-ply shear along mismatched fibre directions (+45 and −45 °) [19, 63], this deformation state promotes prominent mixed-mode (Mode I and Mode II) fracture behaviour in the delamination regions.

The plots in Fig.11 describe the evolution of local strain with increasing axial strain at several representative locations (L1 – L4). At all locations, the local strain exhibits a clear increasing trend with increasing global axial strain. By adopting an approximate apparent yield point of the laminate at ∼ 3.7% based on non-interrupted stress-strain measurements [51], it is evident that room-temperature specimens experience a prominent increase in local strain primarily after the apparent yield point. In contrast, low-temperature specimens show a rapid increase in local strain throughout all three strain steps, indicating an earlier activation of localised deformation mechanisms.

The locations L1 (near the corner) and L2 (in the centre) were situated within Ply 1, which is the surface plies with +45° fibres in the specimens. Similar strain histories can

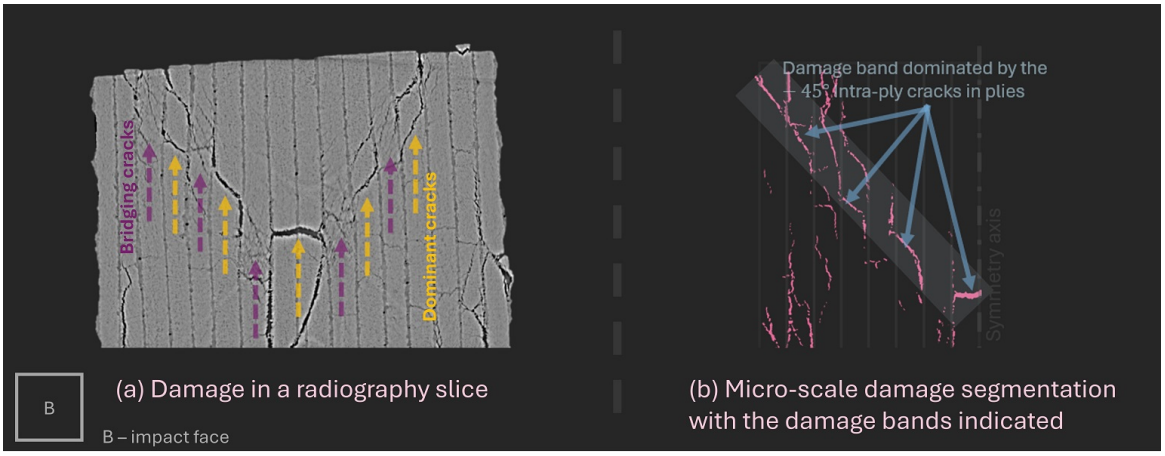

Figure 12: A radiography slice from literature [51] showing the dominant cracks and the bridging cracks: (a) the tomography slice and (b) the segmentation of the opened cracks. The dominant cracks were generated primarily by in-plane shear, and thus, Mode-II dominated. In contrast, the mixed-mode fracture is the driving mechanism of the bridging cracks, which can be small in size and spatially discrete.

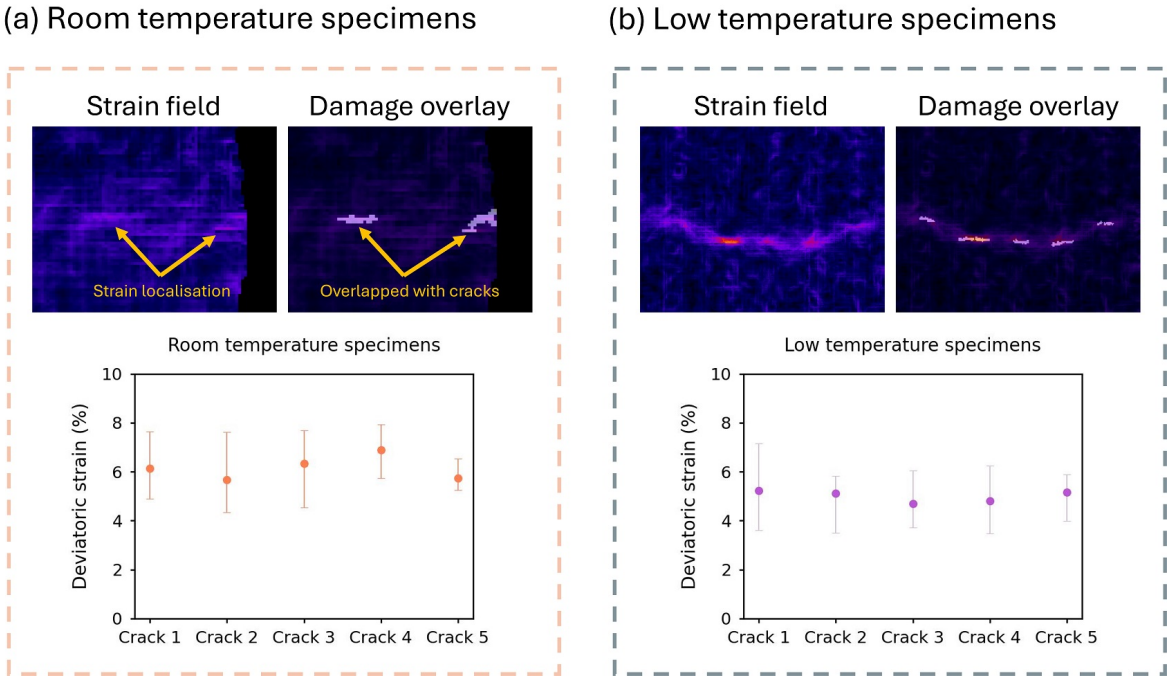

Figure 13: The correlation of the locations between the shear strain localisation and damage regions at (a) room temperature and (b) low temperatures, demonstrating a good consistency. A statistical measurement of the residual strain at the crack tips was performed to evaluate the microscopic strain of matrix cracking under the loading condition.

be found between these two locations, as they belong to the same shear localisation band (see Fig.10). At both locations, the strain response is characterised by Mode-II–dominated cracking aligned with the +45° fibre direction. Location L3 corresponds to the same corner position as L1 but lies within Ply 2, a −45° ply, and therefore aligns with the off-fibre-direction diagonal of that ply (see notations in Fig. 6a). The pronounced strain localisation observed at L3 along the +45° fibre direction indicates significant shear deformation perpendicular to the local fibre orientation (−45°), corresponding to cut-through-fibre shear. This cut-through-fibre shear, in combination with along-fibre shear induced by direct ply compression, drives the initiation of discrete intra-ply cracks distributed along the off-fibre-direction diagonal, as shown in Fig. 9b. Given the comparable contributions of deviatoric and volumetric strain at L3, these discrete intra-ply cracks are likely governed by mixed-mode fracture. The opening component of the fracture is attributed to inter-ply shear coupling and Poisson-driven transverse deformation under global uniaxial compression. Location L4 is situated

within the middle −45° ply cluster, where a high level of shear localisation is already observed at the lowest strain level (CL1), similar to the behaviour in the surface plies. This observation explains the early onset of opened damage in the mid-ply cluster reported in the previous study [51].

In fact, the phenomenon observed at L3 is not confined to a single ply, but can extend across multiple adjacent plies, forming a contiguous through-laminate-thickness shear band (see CL1 – CL3 in Fig. 10a). These cutting-through-fibre shear bands become increasingly prominent in low-temperature specimens and at higher strain levels. The resulting intra-ply cracks distributed along the off-fibre-direction diagonal in −45° fibre plies bridge the dominant intra-ply cracks aligned with the fibre-direction diagonal in +45° fibre plies, giving rise to a continuous damage band across the laminate thickness, as shown in Fig.12, which is observed in the previous study [51]. As a result of shear acting perpendicularly through the fibre direction, these bridging cracks tend to remain small and discrete in size.

Although the magnitude of the shear strain at L3 is lower than that observed at L1, the in-plane shear coupling across the lamination thickness of ±45 CFRP (see CL1 – CL3 in Fig. 10a) clearly showcases the interactive stress transfer between adjacent pies with mismatched fibre orientations. This analysis provides quantitative evidence that the local deformation state departs from the nominal in-plane shear response assumed when interpreting uniaxial tests of ±45 laminates [61], Instead, a pronounced through-thickness gradient develops, characterised by a "mixed-mode" stress-strain state. This mechanistic insight helps rationalise the reported sensitivity of the apparent shear response to specimen geometry and boundary conditions, as well as the macroscopic surface strain non-uniformity measured by full-field techniques [64, 65]. Importantly, while uniaxial loading may lead to an overestimation of the apparent shear stiffness prior to the apparent yield of the laminates [66] due to inter-ply shear coupling and cut-through-fibre shear, the early damage onset and strain localisation in surface plies indicate a spatial non-uniform and temporal unsynchronised stress development across the laminate thickness. This behaviour can, in turn, result in an underestimation of the ply shear strength at failure [61]. Under HSR loading and extreme temperatures, these uncertainties are expected to be further amplified by rate-dependent [26] and temperature-dependent [50] matrix/interface behaviour, as well as fibre-reorientation effects [19], promoting stronger localisation [67] and inter-ply constraint-driven deviations [61] from a uniform shear state.

It is worth noting that, although the present study quantifies residual displacements and strains, these measurements can still be indicative of *in-situ* deformation processes and the associated stress state during loading. This is particularly relevant for epoxy matrices, which typically exhibit a limited elastic regime under HSR loading and/or low temperatures [68, 69, 70]. Under such conditions, localised permanent deformation may develop even when the macroscopic response appears predominantly viscoelastic. This behaviour is driven by pronounced strain localisation and the associated thermal (adiabatic) softening, which can promote irreversible microstructural deformation during loading [71, 72, 73].

By superimposing the segmented damage masks with the deviatoric strain fields (Fig.13), a strong spatial correspondence is observed between the locations of the intra-ply cracks and regions of high strain localisation. Here, the residual strain evaluated in the vicinity of crack tips is used as an indicative measure of the localised deformation retained after unloading. Owing to the limited spatial resolution of the correlation sub-volume and the known challenges of DVC near displacement discontinuities, these values should be interpreted as a conservative proxy for the *in-situ* crack-tip deformation rather than the instantaneous peak strain. Based on five representative cracks, the estimated local residual strain associated with epoxy cracking can reach ∼6% or higher, which is plausible given the reported large-strain deformation capacity of epoxy resins under loading [74, 75].

4. Conclusion

This study demonstrates the application of DVC to CFRP laminates subjected to HSR loading under room- and low-temperature conditions. A systematic workflow encompassing image acquisition, pre-processing, registration, and post-processing was established, enabling robust reconstruction of microscopic displacement/strain fields and subsequent micron-scale crack segmentation and quantification. By combining the segmented damage with the measured local kinematics, the evolution and micro-mechanics of damage under the prescribed loading and environmental conditions were characterised.

The results show that fibre and laminate configurations strongly govern the directionality and localisation of microscopic displacement and strain. Localisation becomes more pronounced at higher interrupted strain levels and at lower temperatures. Compared with room-temperature specimens, the low-temperature specimens exhibit an earlier onset of damage and localised deformation, occurring prior to the apparent laminate yield.

Across all specimens, damage locations show a strong spatial correspondence with regions of high local strain. The primary intra-ply cracks along the fibre-direction diagonals are predominantly Mode-II dominated, whereas the discrete intra-ply cracks distributed along the off-fibre-direction diagonals near specimen corners exhibit mixed-mode characteristics. Inter-ply delamination is associated with a comparatively larger volumetric deformation component, indicating a stronger Mode-I contribution, while remaining mixed-mode in nature. Moreover, the inter-ply kinematic constraint and associated shear coupling between adjacent plies with mismatched fibre orientations under off-axis loading were evidenced and quantified under HSR conditions. In combination with spatial non-uniform and asynchronous development of local deformation through the laminate thickness,

these findings reveal pronounced through-thickness deformation gradients and systematic departures from the nominal in-plane shear state typically assumed when interpreting uniaxial tests of ±45° laminates. This provides a mechanistic basis for the reported sensitivity of apparent shear response to specimen geometry and boundary conditions, while offering guidance for improved characterisation of CFRP shear properties, particularly under HSR loading and extreme temperature conditions.

References

[1] J. V. Calvo, N. Feito, E. Giner, A simplified fatigue characterization of defective CFRP laminates with infrared thermography, Composite Structures 367 (2025).

[2] L. Poggenpohl, H. Holthusen, J. W. Simon, Failure zone homogenization for modeling damage- and debonding-induced softening in composites including gradient-extended damage at finite strains, International Journal of Plasticity 154 (2022).

[3] J. López-Puente, R. Zaera, C. Navarro, The effect of low temperatures on the intermediate and high velocity impact response of CFRPs, Composites Part B: Engineering 33 (2002) 559–566.

[4] C. Chen, C. Zhang, Z. Zhao, Y. Wang, S. C. Wong, Y. Li, Effect of fiber reinforcement and fabrication process on the dynamic compressive behavior of PEEK composites, International Journal of Mechanical Sciences 155 (2019) 170–177.

[5] Z. Zhang, S. Hou, Y. Mao, L. He, X. Han, Rate-related study on the ply orientation of carbon fiber reinforced epoxy composite laminates, International Journal of Mechanical Sciences 188 (2020).

[6] M. Kayrıcı, H. H. Taser, Experimental investigation of the effect of fabric wrapping method and autoclave curing on the mechanical and thermal degradation of carbon nanotube doped and undoped carbon composite pipes, Polymer Composites 45 (2024) 12885–12898.

[7] Y. O. Özkılıç, E. Madenci, A. Safonov, L. Gemi, S. Yazman, Comprehensive evaluation of tensile properties, damage mechanisms, and predictive modeling of pultruded GFRP after elevated temperatures, Composites Part B: Engineering 304 (2025).

[8] M. Demiral, U. Köklü, S. Yazman, L. Gemi, S. Morkavuk, Unveiling the impact resilience of GFRP and CFRP: A cryogenic exploration through experiment and FE simulation, Composites Part B: Engineering 310 (2026).

[9] K. Hamdi, G. Moreau, Z. Aboura, Digital image correlation, acoustic emission and in-situ microscopy in order to understand composite compression damage behavior, Composite Structures 258 (2021).

[10] Y. Wang, M. J. Emerson, K. Conradsen, A. B. Dahl, V. A. Dahl, E. Maire, P. J. Withers, Evolution of fibre deflection leading to kink-band formation in unidirectional glass fibre/epoxy composite under axial compression, Composites Science and Technology 213 (2021) 108929.

[11] Y. Bai, T. Vallée, T. Keller, Delamination of pultruded glass fiber-reinforced polymer composites subjected to axial compression, Composite Structures 91 (2009) 66–73.

[12] A. Pupurs, S. Goutianos, P. Brondsted, J. Varna, Interface debond crack growth in tension-tension cyclic loading of single fiber polymer composites, Composites Part A: Applied Science and Manufacturing 44 (2013) 86–94.

[13] Y. f. Su, T. y. Zhang, H. Sun, L. h. Ma, W. Zhou, Cryogenic damage behavior of carbon fiber reinforced polymer composite laminates via fiber-optic acoustic emission, Composites Part A: Applied Science and Manufacturing 186 (2024).

[14] S. Morkavuk, U. Köklü, M. Bağcı, L. Gemi, Cryogenic machining of carbon fiber reinforced plastic (CFRP) composites and the effects of cryogenic treatment on tensile properties: A comparative study, Composites Part B: Engineering 147 (2018) 1–11.

[15] Y. O. Özkılıç, E. Madenci, L. Gemi, TENSILE AND COMPRESSIVE BEHAVIORS OF THE PULTRUDED GFRP LAMINA, Turkish Journal of Engineering 4 (2020) 169–175.

[16] L. Gemi, U. Köklü, S. Yazman, S. Morkavuk, The effects of stacking sequence on drilling machinability of filament wound hybrid composite pipes: Part-1 mechanical characterization and drilling tests, Composites Part B: Engineering 186 (2020).

[17] L. Gemi, M. Azeem, S. Yazman, M. Kayrıcı, O. Gök, Investigation of Mechanical Properties and Damage Development of Filament Wound GFRP Composite Pipes by Ring Tensile Test, Necmettin Erbakan Üniversitesi Fen ve Mühendislik Bilimleri Dergisi (2024).

[18] F. Erhan, L. Gemi, S. Yazman, S. Morkavuk, U. Köklü, A comprehensive investigation into the influence of variation in the stacking sequence on the mechanical behaviour and drilling machinability of basalt fiber-reinforced composite tubes, Composites Part B: Engineering 299 (2025).

[19] M. C. Serna Moreno, S. Horta Muñoz, Pseudo-ductile effects in ±45° angle-ply CFRP laminates under uniaxial loading: Compression and cyclic tensile test, Composites Part B: Engineering 233 (2022).

[20] J. Fuller, M. R. Wisnom, Pseudo-ductility and damage suppression in thin ply CFRP angle-ply, Composites: Part A (2015) 64–71.

[21] B. Fiedler, C. De Jong, T. Hobbiebrunken, M. Hojo, K. Schulte, Micro/macro-mechanical approach of first ply failure in CFRP, Journal of Materials Science 41 (2006) 6760–6767.

[22] B. P. Wingate, M. W. Czabaj, In-situ imaging of flexure-induced fracture in tape-laminate composites using high-resolution X-ray computed tomography, Composites Science and Technology 220 (2022).

[23] J. P. Hou, C. Ruiz, Measurement of the properties of woven CFRP T300 / 914 at different strain rates, Composites Science and Technology 60 (2000) 2829–2834.

[24] D. Ivančević, J. Ratković, E. Giannaros, Strain rate-dependent failure modelling of impact damage in laminated CFRP structures, Composite Structures 330 (2024).

[25] J. M. Rodríguez-Sereno, J. Pernas-Sánchez, J. A. Artero-Guerrero, J. López-Puente, On the importance of strain rate dependence in high velocity impacts of woven CFRP fragments: Experimental and numerical methodology, International Journal of Impact Engineering 198 (2025).

[26] H. Cui, D. Thomson, A. Pellegrino, J. Wiegand, N. Petrinic, Effect of strain rate and fibre rotation on the in-plane shear response of ±45° laminates in tension and compression tests, Composites Science and Technology 135 (2016) 106–115.

[27] N. Pournoori, G. Corrêa Soares, O. Orell, S. Palola, M. Hokka, M. Kanerva, Adiabatic heating and damage onset in a pultruded glass fiber reinforced composite under compressive loading at different strain rates., International Journal of Impact Engineering 147 (2021).

[28] Z. Song, Z. Wang, H. Ma, H. Xuan, Mechanical behavior and failure mode of woven carbon/epoxy laminate composites under dynamic compressive loading, Composites Part B: Engineering 60 (2014) 531–536.

[29] J. Zhao, L. Guo, L. Zhang, X. Wang, Y. Tang, Z. Li, Experimental investigations on the in-plane dynamic compressive behavior and upper limit of constant strain rate for 2D twill weave carbon fiber reinforced composite, Composites Part B: Engineering 220 (2021).

[30] J. Yu, J. Huang, L. Zhang, S. Yu, L. Guo, T. Huang, Dynamic response and damage mechanisms of 2D plain weave hybrid composites under the out-of-plane punch shear loading, International Journal of Impact Engineering 197 (2025).

[31] J. Liu, Y. Li, M. Huang, Y. Zhang, Y. Lu, L. Dong, Prediction of low-velocity impact mechanical response and damage in thermoplastic composites considering elastoplastic behavior, International Journal of Impact Engineering 194 (2024).

[32] N. Zhang, G. Zhou, X. Guo, S. Xuan, D. Wei, X. Wang, D. Cai, High-velocity impact damage and compression after impact behavior of carbon fiber composite laminates: Experimental study, International Journal of Impact Engineering 181 (2023).

[33] P. Mazzuca, J. P. Firmo, J. R. Correia, E. Castilho, Influence of elevated temperatures on the mechanical properties of glass fibre reinforced polymer laminates produced by vacuum infusion, Construction and Building Materials 345 (2022).

[34] G. Aklilu, S. Adali, G. Bright, Long-term effects of low and high temperatures on the mechanical performance of hybrid FRP composite laminates: Experimental and model assessment, Composites Part C: Open Access 11 (2023).

[35] T. J. Katafiasz, E. S. Greenhalgh, G. Allegri, S. T. Pinho, P. Robinson, The influence of temperature and moisture on the mode I fracture toughness and associated fracture morphology of a highly toughened aerospace CFRP, Composites Part A: Applied Science and Manufacturing 142 (2021).

[36] J. Körbelin, N. Junge, B. Fiedler, Modelling of low-velocity impact and compression after impact of CFRP at elevated temperatures, Composites Part A: Applied Science and Manufacturing 147 (2021).

[37] S. Sánchez-Sáez, T. Gómez-Del Río, E. Barbero, R. Zaera, C. Navarro, Static behavior of CFRPs at low temperatures, Composites: Part B 33 (2002) 383–390.

[38] Y. Li, J. Meng, G. Niu, H. Yang, P. Wang, H. Lei, D. Fang, Cryogenic damage mechanisms of CFRP laminates based on in-situ X-ray computed tomography characterization, Composites Science and Technology 247 (2024) 110413.

[39] Y. Bai, Z. Zhao, S. Duan, P. Wang, Y. Li, H. Lei, Internal shear damage evolution of CFRP laminates ranging from -100 °C to 100 °C using in-situ X-ray computed tomography, Composites Science and Technology 259 (2025).

[40] S. Lee, E. Jo, W. Ji, Digital volume correlation technique for characterizing subsurface deformation behavior of a laminated composite, Composites Part B: Engineering 194 (2020).

[41] S. Hong, Z. Yuan, D. Pan, C. Kuang, B. Dong, S. Fan, Digital-volume-correlation-assisted crack extraction using X-ray computed tomography images of cementitious materials, Cement and Concrete Composites 158 (2025).

[42] Y. Wang, Q. Chen, Q. Luo, Q. Li, G. Sun, Characterizing damage evolution in fiber reinforced composites using in-situ X-ray computed tomography, deep machine learning and digital volume correlation (DVC), Composites Science and Technology 254 (2024).

[43] C. Kuang, S. Ghosh, A. Michel, Enhanced detection of fine damage in composite materials using integrated X-ray computed tomography, digital volume correlation, and U-Net, Journal of Building Engineering 98 (2024).

[44] M. Mehdikhani, C. Breite, Y. Swolfs, J. Soete, M. Wevers, S. V. Lomov, L. Gorbatikh, Digital volume correlation for meso/micro in-situ damage analysis in carbon fiber reinforced composites, Composites Science and Technology 213 (2021).

[45] H. Zhang, L. Yang, S. Ren, K. Wang, J. Li, In-situ experimental characterization and numerical investigation of the crack initiation of SMC composite under uniaxial tension, Composites Part A: Applied Science and Manufacturing 188 (2025).

[46] L. Jiang, H. Xiong, T. Zeng, J. Wang, S. Xiao, L. Yang, In-situ micro-CT damage analysis of carbon and carbon/glass hybrid laminates under tensile loading by image reconstruction and DVC technology, Composites Part A: Applied Science and Manufacturing 176 (2024).

[47] T. J. Pirzada, D. Liu, J. Ell, H. Barnard, I. Šulák, M. Galano, T. J. Marrow, R. O. Ritchie, In situ observation of the deformation and fracture of an alumina-alumina ceramic-matrix composite at elevated temperature using x-ray computed tomography, Journal of the European Ceramic Society 41 (2021) 4217–4230.

[48] F. Léonard, J. Stein, C. Soutis, P. J. Withers, The quantification of impact damage distribution in composite laminates by analysis of X-ray computed tomograms, Composites Science and Technology 152 (2017) 139–148.

[49] D. J. Bull, S. M. Spearing, I. Sinclair, L. Helfen, Three-dimensional assessment of low velocity impact damage in particle toughened composite laminates using micro-focus X-ray computed tomography and synchrotron radiation laminography, Composites Part A: Applied Science and Manufacturing 52 (2013) 62–69.

[50] X. Sun, D. Sory, K. Liu, B. Lukić, D. Simonian, K. L. Wong, A. Rack, D. Chapman, N. Petrinic, D. Eakins, Effect of temperature on high strain-rate damage evolving in CFRP studied by synchrotron-based MHz X-ray phase contrast imaging, Composites Part B: Engineering 279 (2024).

[51] X. Sun, B. Lukić, K. Liu, D. Sory, M. Lißner, J. Hoffmann, D. Chapman, N. Petrinic, D. Eakins, Role of temperature in the development of micro-scale damage in CFRP laminates through interrupted high-rate loading and synchrotron phase-contrast μ-CT, Composites Part A: Applied Science and Manufacturing 200 (2026) 109284.

[52] L. Q. Reyes, S. R. Swan, H. Gan, S. M. Seraji, J. Zhang, R. J. Varley, The role of β relaxations in determining the compressive properties of an epoxy amine network modified with POSS and mono-functional epoxy resins, Polymer Testing 93 (2021).

[53] D. J. Bull, L. Helfen, I. Sinclair, S. M. Spearing, T. Baumbach, A comparison of multi-scale 3D X-ray tomographic inspection techniques for assessing carbon fibre composite impact damage, Composites Science and Technology 75 (2013) 55–61.

[54] Comet Technologies Canada Inc., Dragonfly 3D World (Version 2025.1), 2025.

[55] A. Fedorov, R. Beichel, J. Kalpathy-Cramer, J. Finet, J. C. Fillion-Robin, S. Pujol, C. Bauer, D. Jennings, F. Fennessy, M. Sonka, J. Buatti, S. Aylward, J. V. Miller, S. Pieper, R. Kikinis, 3D Slicer as an image computing platform for the Quantitative Imaging Network, Magnetic Resonance Imaging 30 (2012) 1323–1341.

[56] O. Stamati, E. Andò, E. Roubin, R. Cailletaud, M. Wiebicke, G. Pinzon, C. Couture, R. Hurley, R. Caulk, D. Caillerie, T. Matsushima, P. Bésuelle, F. Bertoni, T. Arnaud, A. Laborin, R. Rorato, Y. Sun, A. Tengattini, O. Okubadejo, J.-B. Colliat, M. Saadatfar, F. Garcia, C. Papazoglou, I. Vego, S. Brisard, J. Dijkstra, G. Birmpilis, spam: Software for Practical Analysis of Materials, Journal of Open Source Software 5 (2020) 2286.

[57] M. E. Gurtin, An introduction to continuum mechanics, volume 158, Academic Press, New York, 1981.

[58] J. Schindelin, I. Arganda-Carreras, E. Frise, V. Kaynig, M. Longair, T. Pietzsch, S. Preibisch, C. Rueden, S. Saalfeld, B. Schmid, J. Y. Tinevez, D. J. White, V. Hartenstein, K. Eliceiri, P. Tomancak, A. Cardona, Fiji: An open-source platform for biological-image analysis, 2012.

[59] J. AHRENS, B. GEVECI, C. LAW, ParaView: An End-User Tool for Large-Data Visualization, in: Visualization Handbook, Elsevier, 2005, pp. 717–731.

[60] R. M. Hackett, Polar Decomposition, in: Hyperelasticity Primer, Springer International Publishing, Cham, 2018, pp. 9–18.

[61] ASTM, D3518 - Test Method for In-Plane Shear Response of Polymer Matrix Composite Materials by Tensile Test of a 45 Laminate, Technical Report, ASTM, West Conshohocken, PA, 2018.

[62] T. Matsuda, K. Goto, N. Kubota, N. Ohno, Negative through-the-thickness Poisson's ratio of elastic-viscoplastic angle-ply carbon fiber-reinforced plastic laminates: Homogenization analysis, International Journal of Plasticity 63 (2014) 152–169.

[63] M. Burhan, T. Scalici, Z. Ullah, Z. Kazancı, G. Catalanotti, A three-dimensional Finite Fracture Mechanics model to predict free edge delamination in angle-ply laminates, Engineering Fracture Mechanics 306 (2024).

[64] Y. Long, C. Qi, R. Han, C. Guo, H. Qiao, W. Hao, Influence of width on the tensile properties of ±45° fiber-reinforced composites using DIC and AE, Materials and Design 261 (2026).

[65] M. Merzkirch, Q. An, A. M. Forster, In-Plane Shear Response of GFRP Laminates by ± 45° and 10° Off-axis Tensile Testing using Digital Image Correlation, Technical Report, National Institute of Standards and Technology, Gaithersburg, 2019.

[66] S. Horta Muñoz, M. C. Serna Moreno, Tension–compression biaxial test with ±45° symmetric angle-ply laminates for determining the pure shear response in principal material directions of a lamina, Composites Part B: Engineering 261 (2023).

[67] A. Chakraborty, S. Roy, Shear localization and shear banding: A review about the complex interplay between material, microstructural and process variables, 2024.

[68] J. C. Griffith, S. Wang, D. R. Palubiski, K. R. Ramakrishnan, S. Rochat, F. Giuliani, M. Walls-Bruck, I. Hamerton, Investigating the microcracking behaviour of a commercial epoxy matrix under

cryogenic conditions, Composites Part A: Applied Science and Manufacturing 199 (2025).
[69] C. P. Buckley, J. Harding, J. P. Hou, C. Ruiz, A. Trojanowski, Deformation of thermosetting resins at impact rates of strain. Part I: Experimental study, Journal of the Mechanics and Physics of Solids 49 (2001) 1517–1538.
[70] P. Bhagoria, M. R. Bharadwaj, R. Kumar, K. Yadav, V. Tiwari, Mechanical and fracture behaviour of epoxy polymer under extreme low temperature and high strain rate conditions, International Journal of Adhesion and Adhesives 140 (2025).
[71] Z. Xia, X. Shen, F. Ellyin, An assessment of nonlinearly viscoelastic constitutive models for cyclic loading: The effect of a general loading/unloading rule, Mechanics of Time-Dependent Materials 9 (2005) 281–300.
[72] O. Starkova, S. T. Buschhorn, E. Mannov, K. Schulte, A. Aniskevich, Creep and recovery of epoxy/MWCNT nanocomposites, Composites Part A: Applied Science and Manufacturing 43 (2012) 1212–1218.
[73] D. J. Plazek, The Temperature Dependence of the Viscoelastic Behavior of Poly(vinyl acetate), Polymer Journal 12 (1980) 43–53.
[74] R. Kumar, P. Bhagoria, M. R. Bharadwaj, V. Tiwari, From quasi-static to dynamic: Experimental study of mechanical and fracture behaviour of epoxy resin, International Journal of Impact Engineering 195 (2025).
[75] R. K. Goldberg, G. D. Roberts, Strain Rate Sensitivity of Epoxy Resin in Tensile and Shear Loading, Technical Report, National Aeronautics and Space Administration, 2005.